Inorganic Chemistry

Article

pubs.acs.org/IC

Tunable Energy Transfer Rates via Control of Primary, Secondary, and Tertiary Structure of a Coiled Coil Peptide Scaffold

Dale J. Wilger,[†] Stephanie E. Bettis,[†] Christopher K. Materese,[†] Maria Minakova,[†] Garegin A. Papoian,*[,‡] John M. Papanikolas,*[,†] and Marcey L. Waters*[,†]

[†]Department of Chemistry, CB 3290, University of North Carolina, Chapel Hill, North Carolina 27599, United States

[‡]Department of Chemistry and Biochemistry, University of Maryland, College Park, Maryland 20742, United States

Supporting Information

ABSTRACT: Herein we report energy transfer studies in a series of Ru(II) and Os(II) linked coiled-coil peptides in which the supramolecular scaffold controls the functional properties of the assembly. A general and convergent method for the site-specific incorporation of bipyridyl Ru(II) and Os(II) complexes using solid-phase peptide synthesis and the copper-catalyzed azide−alkyne cycloaddition is reported. Supramolecular assembly positions the chromophores for energy transfer. Using time-resolved emission spectroscopy we measured position-dependent energy transfer that can be varied through changes in the sequence of the peptide scaffold. High level molecular dynamics simulations were used in conjunction with the spectroscopic techniques to gain molecular-level insight into the observed trends in energy transfer. The most efficient pair of Ru(II) and Os(II) linked peptides as predicted by molecular modeling also exhibited the fastest rate of energy transfer (with $k_{EnT} = 2.3 \times 10^7\ s^{-1}$ (42 ns)). Additionally, the emission quenching for the Ru(II) and Os(II) peptides can be fit to binding models that agree with the dissociation constants determined for the peptides via chemical denaturation.

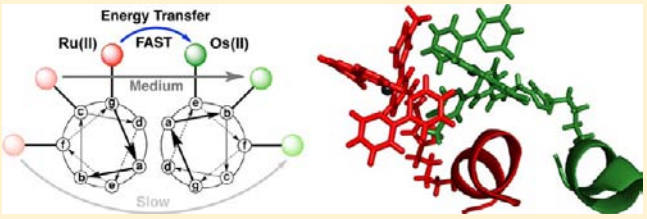

I. INTRODUCTION

The design of molecular materials capable of performing complex functions is pivotal to "bottom-up" approaches in molecular electronics,[1] sensing,[1a,2] and solar energy conversion.[3,4] The most common strategy for building artificial assemblies uses covalent bond formation to connect molecular components with rigid linkers that dictate both distance and orientation. While this approach provides exquisite control over spatial parameters,[5] the optimization of functional performance often requires the development of new synthetic routes making the implementation very difficult, especially as the number of molecular components increases. Alternatively, chromophores have been placed on easily synthesized scaffolds such as polymers,[6] dendrimers,[1a,3c,7] and organogels.[8] However this approach can yield assemblies that are not monodisperse in molecular weight or chemical composition and incorporate many different morphological constituents. While large systems are readily made and some control over the primary structure is possible, the flexible scaffolds result in solution structures that vary from one assembly to the next.

Another approach to achieve functional architectures draws inspiration from natural systems, which combine simple molecular building-blocks to form highly complex functional systems. Nature exploits relatively weak noncovalent interactions to achieve functional architectures with a hierarchical control, in which sequence defines structure and self-assembly, which defines function. Proteins, lipids, and oligonucleotides form the structural framework that organize functional elements in spatial proximity and with well-defined orientations.[9] To this end, functionalized biological molecules such as oligonucleotides,[10] amyloid-like peptide fibrils,[11] and even derivatized virus coated proteins have been designed and investigated as functional materials.[12] These types of designed systems[11,13−15] that mimic the organizational strategies of biomolecules provide a number of advantages, including design flexibility, ease of synthesis, and spatial control of functionality through *supramolecular architectures* that allow for fine-tuning of materials properties.

Herein we report the design of an artificial polypeptide system based on a heterodimeric coiled-coil architecture in which the primary sequence defines both the secondary and the tertiary structure, resulting in self-assembly, which provides fine control of the positioning of octahedral tris(bipyridyl) transition metal complexes $[M^{II}(bpy)_3]^{2+}$ (M = Ru or Os, bpy = 2,2′-bipyridyl). Coiled-coils are a common protein motif and provide structural architecture for many important protein scaffolds including α-keratin[16] and tropomyosin.[17] Moreover, the sequence-structure rules are well-defined, allowing for the design of highly tunable supramolecular architectures by control of the primary sequence.[18a] In this study we demonstrate the ability of the peptide secondary structure to control self-assembly and hence relative positioning of the octahedral complexes, resulting in systematic tuning of the energy transfer properties of the system. The Ru(II) and Os(II) metal complexes are positioned near the midpoints of two

Received: March 30, 2012
Published: June 8, 2012

dx.doi.org/10.1021/ic300669t | Inorg. Chem. 2012, 51, 11324−11338

complementary peptide chains, each consisting of 28 residues (Figure 1). The primary sequence of each chain is chosen such

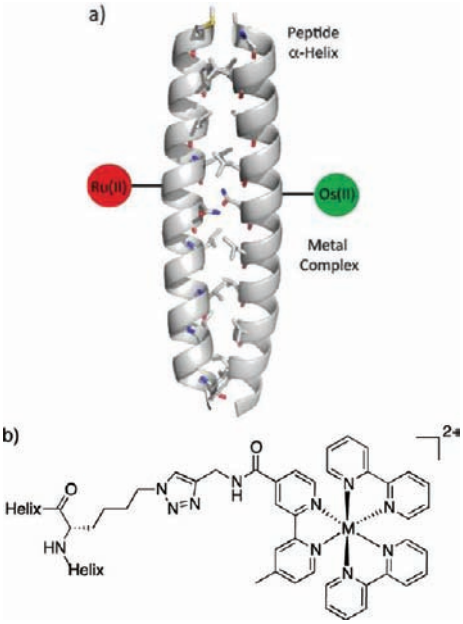

Figure 1. (a) Illustration of metallopeptide system containing the α-helical coiled-coil scaffold and metal complexes (coiled coil: pdb 2AHP). (b) Structure of the metal complex and its attachment to the α-helix.

that they adopt a dimeric supramolecular structure consisting of two α-helical coils, in which the hydrophobic residues are shielded from the aqueous environment and the hydrogen bonding and ionic interactions are maximized. Photoexcitation of the Ru(II) complex in the folded assembly results in energy transfer to the lower energy Os(II) acceptor on the opposing chain. Since the metal complexes are placed on different peptide chains, energy transfer is only possible if the two chains associate in solution, making this system particularly sensitive to the secondary and tertiary structure of the peptide scaffold.

The peptide structures studied here take advantage of two flexible synthetic methodologies: solid-phase peptide synthesis (SPPS) and the copper(I)-catalyzed azide–alkyne cycloaddition (CuAAC or "click reaction"). SPPS is advantageous as it allows for exact positioning of the chromophores in the primary sequence. The use of click chemistry as an orthogonal linkage strategy between the chromophores and the peptides has several advantages. First, it avoids issues with formation of statistical mixtures of species, as was obtained in the electron transfer coiled-coil systems developed by Ogawa, in which the chromophore linkage was accomplished via nonspecific coordination chemistry.[15] Second, click chemistry provides advantages over the direct amide linkage used in the electron-transfer oligoproline systems reported by Meyer, in which orthogonal protecting group strategies had to be employed.[14]

We have examined a series of peptide assemblies that systematically vary the placement of the complexes along the peptide backbone, results in predictable changes in the energy transfer rate, which are measured using time-resolved emission methods. Variation in the rate by almost an order of magnitude across the series, as well as denaturation studies, confirm that energy transfer is the direct result of folding into a well-defined tertiary structure. All-atom molecular dynamics simulations provide insight into the microscopic environment, revealing an assembly with a dynamic, yet robust, tertiary structure that effectively controls the relative positioning of the two complexes.

II. RESULTS AND DISCUSSION

System Design. Since energy transfer between Ru(II) and Os(II) polypyridine complexes has not been previously studied using this type of chemical scaffold, a number of design elements were considered crucial for the proper development of such a system, as discussed below: (1) the design of the coiled-coil peptide scaffold, (2) the attachment chemistry including its utility, versatility, and compatibility with standard conditions for automated peptide synthesis, (3) the nature of the metal complexes including their chemical stability and photophysical properties, (4) the nature of the linking group and how it may affect coiled-coil secondary and quaternary structure, and (5) the positions for Ru(II) and Os(II) modification within the coiled-coil peptides.

Coiled-Coil Peptide Scaffold Design. The coiled-coil peptide scaffold was adopted from the heterodimeric self-assembling fiber (SAF) system originally reported by Woolfson and co-workers (Figure 2).[18] Both 28-residue peptides contain

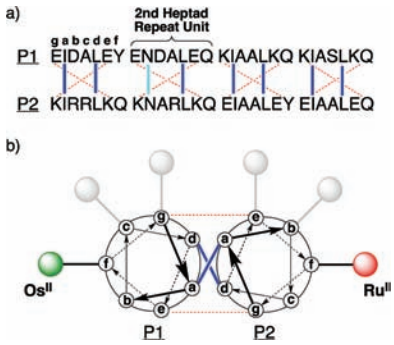

Figure 2. (a) Primary sequences of the P1 and P2 peptides using the single letter amino acid code (in capitals). Each 28-residue peptide has four heptad repeat units. The common letter designations for the heptad positions (***abcdefg***) are shown above the first heptad repeat unit for P1. The hydrophobic interactions are shown as blue lines, the hydrogen bonding interaction between Asn side chains is shown as a cyan line, and the complementary ionic interactions between the two peptides are shown as red dashed lines. (b) A helical-wheel diagram displaying the potential points for attachment when viewed down helix axis from the N-terminus. The P1 peptide is modified with Os(II) at the ***f***, ***c***, or ***g*** position within the second heptad. The P2 peptide is modified with Ru(II) at the ***f***, ***b***, or ***e*** position within the second heptad.

the canonical repeating heptad sequence (designated ***abcdefg***) that most coiled-coil peptides display. The ***a*** and ***d*** sites are reserved for hydrophobic residues which provide the primary driving force for dimerization. Isoleucine and leucine residues were specifically chosen for the ***a*** and ***d*** sites, respectively, because they have been shown superior promoters for the desired parallel dimeric structure.[18a,19] The ***e*** and ***g*** positions contain oppositely charged residues such as lysine and glutamate that provide complementary interactions only when the heterodimeric and parallel partnering is considered.[19c,20] An asparagine residue is included at a single ***a*** position within each sequence. Polar residues included at these positions must satisfy their hydrogen bonding potential, and impart folding specificity

dx.doi.org/10.1021/ic300669t | Inorg. Chem. 2012, 51, 11324–11338

through mutual alignment to give a parallel coiled-coil exclusively.[19,20b,21] Although the incorporation of two asparagine residues within the hydrophobic core of the parallel dimer interface is slightly destabilizing compared to more hydrophobic residues at these positions, their incorporation is more destabilizing within undesired structures including trimers, tetramers, antiparallel dimers, and misaligned dimers.[19,20b,21] Thus, this sequence design provides parallel heterodimeric coiled-coils to the exclusion of other supramolecular architectures. Of significance for this study is the fact that the monomeric peptides with this type of sequence design typically do not fold into helical structures to any great extent. This is attributed to the fact that such a monomeric helix would display a large hydrophobic patch on one face of the helix, which is unfavorable in aqueous solution.

The majority of Woolfson's SAF peptides contain complementary interactions that promote a staggered heterodimer structure referred to as the "sticky-ends" design.[18b] The P1 peptide sequence is a permutation which has been rearranged to discourage longitudinal association, and therefore fiber formation.[18b] Natural coiled-coil peptides all share this "blunt" end assembly.[22] The P2 apopeptide sequence remains unchanged from several of Woolfson's reports.[18]

Synthesis of Metallopeptides Using CuAAC. A number of redox-active amino acids containing Ru(II) and Os(II) bipyridyl complexes have previously been reported.[14,23] These amino acid derivatives are convenient because they can be incorporated into metallopeptides during traditional linear solid-phase peptide synthesis (SPPS), although they often include longer coupling times, more exotic coupling reagents, and decreased yields. We chose a convergent synthetic strategy because it would allow for the peptide, linker, and bipyridyl complexes to be easily varied for later optimization and investigation. The Cu(I)-catalyzed azide–alkyne 1,3-dipolar cycloaddition provides general and robust conditions for the conjugation of biomolecules.[24] Several alkynyl-functionalized Ru(II) and Os(II) complexes have been reported,[10a–c,25] having previously been used for oligonucleotide modification with Sonogashira Pd(0) cross-coupling chemistry.[26] The Ru(II) and Os(II) bipyridyl complexes **1a** and **1b** (Figure 3) were selected,[25] as opposed to previously described phenanthroline complexes,[10a–c] because the sp^3-hybridized carbon within the propargyl amide group increases flexibility and electronically

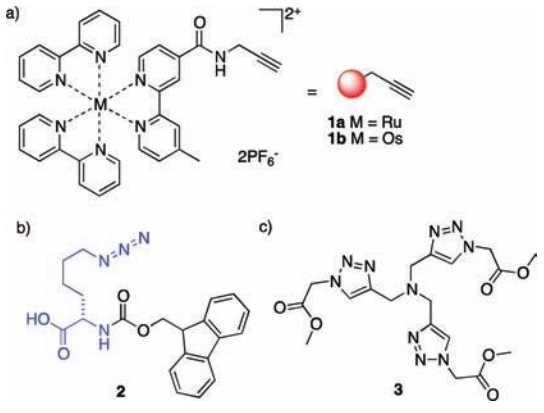

Figure 3. (a) Alkynyl-functionalized Ru(II) and Os(II) containing complexes **1a** and **1b**, respectively. (b) Fmoc-lysine-ε-azide **2** used in the synthesis of azidopeptides. (c) *tris*-(Triazolylmethyl)amine ligand **3** used to accelerate the CuAAC conjugation reaction.

decouples the metallobipyridine from the triazole ring formed during the CuAAC reaction.

Lysine ε-azide was selected to provide the tether for **1a** and **1b** since it contains four aliphatic methylene units, and was anticipated to be less destabilizing toward the coiled-coil peptide structure compared to shorter tether lengths (Figure 3).[18f,27] The linker was also selected to be sufficiently flexible so as to allow rotational freedom for the metal complexes since orientation and angular relationships between donor and acceptor modules have a strong influence on energy transfer efficiencies.[10c,d,13a]

Azidopeptides were synthesized by incorporating Fmoc-lysine ε-azide (**2**) at the desired point of (donor/acceptor) attachment during SPPS (Scheme 1). After the azidopeptides

Scheme 1. Synthesis of Metallopeptides Using CuAAC[a]

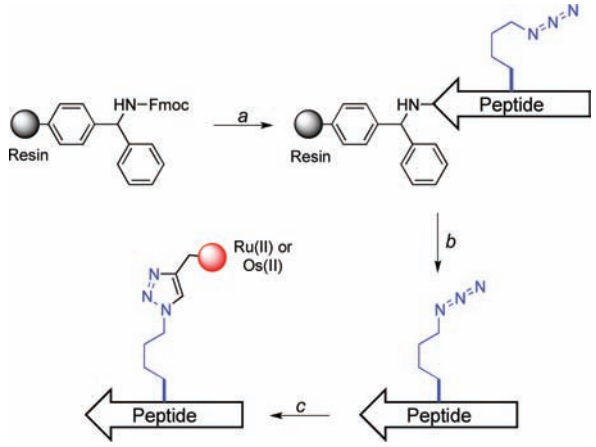

[a]Conditions: (a) solid-phase peptide synthesis: Fmoc removal, piperidine/DMF (1:4); 2 × 15 min; coupling, 4 equiv of amino acid, 4 equiv of HBTU, 4 equiv of HOBT, 4 equiv of DIPEA, DMF; capping, Ac_2O/2,6-lutidine/DMF (5:6:89); (b) cleavage, TIPS/H_20/TFA (2.5:2.5:95); purification, RP-HPLC (c) conjugation using the CuAAC reaction, 2 equiv of **1a** or **1b**, 1.5–2 equiv of $[Cu(CH_3CN)_4]$-PF_6, 1 equiv of **3**, DMF/buffer (1:1), buffer =10 mM sodium phosphate buffer, pH 8.5.

were cleaved from the solid-phase support and purified using RP-HPLC, they were conjugated to **1a** or **1b** using the CuAAC reaction (Scheme 1). Reactions containing a *tris*-(triazolylmethyl)amine ligand (**3**) demonstrated shorter reaction times and increased yields compared to reactions lacking the ligand.[28] A more basic reaction medium (pH 8.5) provided shorter reaction times compared to lower pH media.[24c] After conjugation was complete, the metallopeptides were purified using a combination of size-exclusion chromatography and RP-HPLC as described below.

Donor/Acceptor Placement in the Coiled-Coil. The coiled-coil peptide scaffold contains a multitude of possible positions for the attachment of polypyridyl donor/acceptor complexes. The positions selected for modification were chosen to provide a range of well-defined donor/acceptor distances in the self-assembled coiled-coil for measuring excited-state energy transfer. Substitutions on the first and last heptad repeat units of the peptides could potentially result in complications from end fraying near the termini, and were therefore avoided. Conjugation of **1b** (Os(II)) at the 2*f*, 2*c*, or 2*g* position within the P1 peptide sequence gave the excited state energy acceptor metallopeptides 2*f*-Os-P1, 2*c*-Os-P1, and 2*g*-Os-P1, respectively

dx.doi.org/10.1021/ic300669t | *Inorg. Chem.* 2012, 51, 11324–11338

(Table 1). Similarly, conjugation of **1a** (Ru(II)) at the 2*f*, 2*b*, or 2*e* position within the P2 peptide sequence provided the donor

Table 1. Ru(II) and Os(II) Metallopeptide Sequences[a]

Peptide	Sequence[a]
P1	EIDALEY-ENDALEQ-KIAALKQ-KIASLKQ
2*f*-Os-P1	EIDALEY-ENDALEX-KIAALKQ-KIASLKQ
2*c*-Os-P1	EIDALEY-ENDXLEQ-KIAALKQ-KIASLKQ
2*g*-Os-P1	EIDALEY-XNDALEX-KIAALKQ-KIASLKQ
P2	KIRRLKQ-KNARLKQ-EIAALEY-EIAALEQ
2*f*-Ru-P2	KIRRLKQ-KNARLKX-EIAALEY-EIAALEQ
2*b*-Ru-P2	KIRRLKQ-KNXRLKQ-EIAALEY-EIAALEQ
2*e*-Ru-P2	KIRRLKQ-KNARLXQ-EIAALEY-EIAALEQ

[a]The primary sequences for the peptides synthesized and characterized in this study are given using the single letter amino acid code (in capitals). X represent the artificial amino acid lysine ε-azide used for the attachment of Os(II) (green) or Ru(II) (red) complexes.

metallopeptides 2*f*-Ru-P2, 2*b*-Ru-P2, and 2*e*-Ru-P2, respectively (Table 1). Three specific pairs of metallopeptides were selected for structural analysis, photophysical characterization, and all-atom molecular dynamics simulation. The 2*f*-Os/2*f*-Ru metallopeptide pair refers to the heterodimer formed by the 2*f*-Os-P1 and 2*f*-Ru-P2 metallopeptides and was expected to provide the largest donor/acceptor separation distance, based on the analysis of parallel dimeric coiled-coils with crystal structures reported in the protein database (PDB code: 3NM6, 1UIX, and 3M9B). The distance between the α-carbons of aligned f positions to 14.9 Å in these crystal structures. Similar analysis indicated that ***b*-*c*** separations were 12.7−13.5 Å, and ***e*-*g*** separations were 9.6−10.3 Å. Although these measurements do not account for the length or flexibility of the azidolysine linker, they qualitatively represent the general trends that may be expected for the rates of energy transfer in the 2*f*-Os/2*f*-Ru, 2*c*-Os/2*b*-Ru, and 2*g*-Os/2*e*-Ru metallopeptide pairs.

Structural Characterization of the Metallopeptide Heterodimers by Circular Dichroism. Circular dichroism (CD) is a common technique for the characterization of peptide secondary structure.[29a] A well-formed α-helix exhibits a maximum in the CD spectrum below 200 nm and minima at 208 and 222 nm. The CD spectra of the monomeric peptides each exhibit relatively weak minima at 208 and 222 nm, characteristic of a dynamic partially folded helical structure, as expected (Figure 4). Because peptide CD spectra are typically plotted with concentration-independent mean residue ellipticity on the *y*-axis, a 1:1 mixture of complementary peptides is expected to exhibit deeper minima at 208 and 222 nm if an α-helical coiled-coil structure is formed, whereas if dimerization does not occur, the spectrum of the mixture will be identical to the average of the spectra for the two individual peptides. The CD spectra for all three heterodimeric metallopeptide pairs indicate that they form coiled-coil structures when mixed in a 1:1 ratio in aqueous buffer at μM concentrations (Figure 4).[29] The ellipticity at 222 nm is a quantitative measure of α-helicity and can be used to monitor coiled-coil dimerization. All three pairs display maximum α-helicity when equimolar mixtures are measured, indicating that heterodimeric coiled-coil structures are being formed (see Supporting Information). The 2*f*-Os/2*f*-Ru peptide pair exhibits the largest negative signal at 222 nm, with an ellipticity ratio for the 2*f*-Os/2*f*-Ru pair at 208 and 222 nm, $\theta_{222}/\theta_{208}$, equal to 1.00. Similarly, the 2*c*-Os/2*b*-Ru and 2*g*-Os/2*e*-Ru peptide pairs both have $\theta_{222}/\theta_{208}$ values equal to

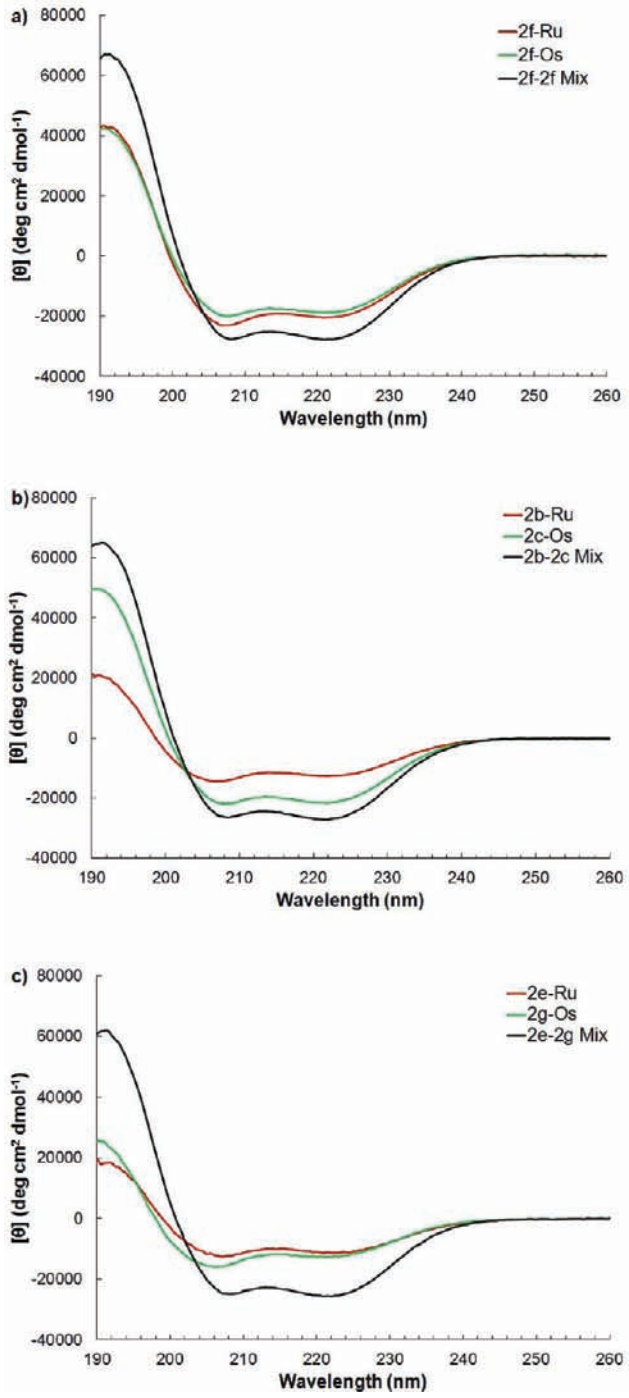

Figure 4. (a) Circular dichroism (CD) spectra of the individual 2*f*-Os (green) and 2*f*-Ru (red) peptides, both at a concentration of 50 μM at 25 °C in 10 mM sodium phosphate buffer, pH 7.4. A 1:1 mixture of the two peptides (black, 50 μM combined peptide concentration) shows a more intense negative signal at 222 nm indicating an increase in the α-helicity for the two peptides. (b) CD spectra of the 2*c*-Os (green) and 2*b*-Ru (red) peptides and the 1:1 mixture (black) under the same conditions as in (a). (c) CD spectra of the 2*g*-Os (green) and 2*e*-Ru (red) peptides and the 1:1 mixture (black) under the same conditions as in (a).

1.03. This ratio is characteristic of dimeric coiled-coil peptides, as single-stranded α-helices have values closer to 0.85.[30]

Thermodynamic Stability Determined Using Guanidinium Denaturation. Chemical denaturation using guanidi-

dx.doi.org/10.1021/ic300669t | *Inorg. Chem.* 2012, 51, 11324−11338

nium chloride (GndHCl) provides a reliable tool for measuring coiled-coil dissociation constants.[20c,31] The method has been used to compare small structural variations within families of similarly designed coiled-coils.[20c] Gibbs free energy change of unfolding (ΔG_{unfold}) was measured for each of the metallopeptide dimers using the method of linear extrapolation (Figure 5).[31] The different donor/acceptor modification points

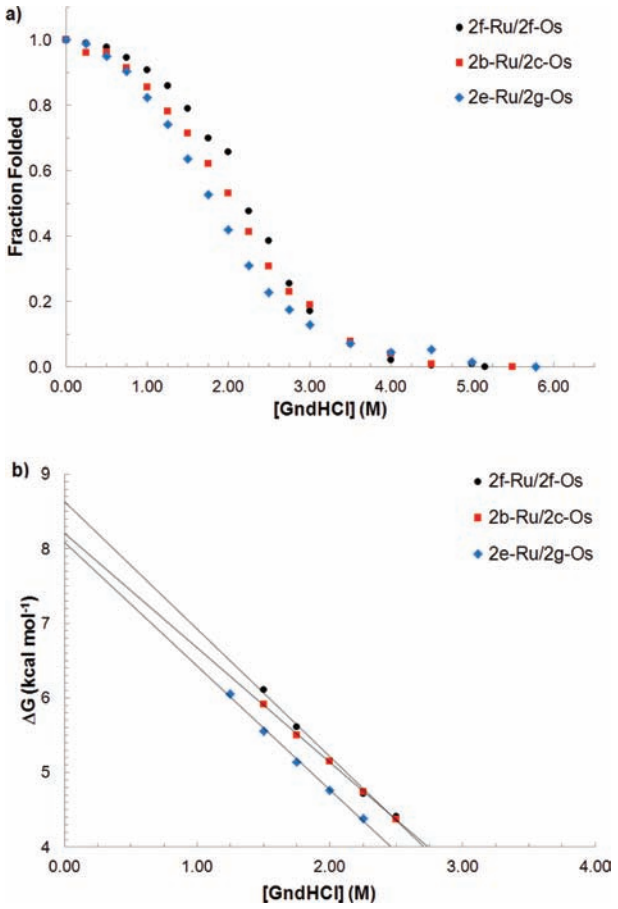

Figure 5. (a) Guanidinium chloride denaturation curves at 25 °C in 20 mM sodium phosphate buffer, 100 mM NaCl, pH 7.4. Data plotted for the 2*f*-Os/2*f*-Ru pair (black circles, 300 μM), the 2*c*-Os/2*b*-Ru pair (red squares, 200 μM), and the 2*g*-Os/2*e*-Ru pair (blue diamonds, 200 μM). The calculation of fraction folded is described within the experimental procedures section. (b) Gibbs free energy of unfolding is plotted as a function of guanidinium chloride concentration ($\Delta G = m[\text{GndHCl}] + \Delta G_{unfold}$). Linear extrapolation (Experimental Section) gives the value of ΔG_{unfold} at zero denaturant concentration. Data shown for the 2*f*-Os/2*f*-Ru pair (black circles, $m = -1.7$ kcal/mol·M, $R^2 = 0.997$), the 2*c*-Os/2*b*-Ru pair (red squares, $m = -1.5$ kcal/mol·M, $R^2 = 0.999$), and the 2*g*-Os/2*e*-Ru pair (blue diamonds, $m = -1.7$ kcal/mol·M, $R^2 = 0.997$).

for the metallopeptide pairs resulted in only subtle differences in structural stability. As may be expected, the 2*f*-Os/2*f*-Ru pair formed the most thermodynamically favorable heterodimer (Table 2). The value of ΔG_{unfold} measured for the 2*f*-Os/2*f*-Ru pair, 8.6 ± 0.10 kcal/mol, corresponds to a dissociation constant (K_d) equal to 0.49 ± 0.09 μM. The α-helicity of the fully folded 2*f*-Os/2*f*-Ru dimer was calculated to be 80%, based on molar ellipticity measurements at 222 nm (−28,600 ± 800 deg·cm^2·dmol^{-1}). The α-helical content determined for the 2*f*-Os/2*f*-Ru dimer falls within the range reported for similar

Table 2. Thermodynamic Stability of the Metallopeptide Heterodimers

peptide pair	ΔG_{unfold} (kcal/mol)[a]	K_d [μM][b]	α-helicity[c]
2*f*-Os/2*f*-Ru	8.6	0.49 ± 0.09	80%
2*c*-Os/2*b*-Ru	8.2	0.97 ± 0.2	74%
2*g*-Os/2*e*-Ru	8.0	1.4 ± 0.3	72%

[a]Gibbs free energy of unfolding (ΔG_{unfold}) was measured for each peptide pair using the linear extrapolation method (Experimental Section). Error estimated to be ±0.10 kcal/mol based on error due to linear extrapolation. [b]Dissociation constants (K_d) were calculated using the equation $\Delta G_{unfold} = -RT$ Ln K_d, using ΔG_{unfold} values obtained by the linear extrapolation method. [c]Maximum ellipticity values for each pair were measured using the CD signal at 222 nm for multiple trials. The predicted maximum molar ellipticity for a 28 residue helix (X_H^{28}) is calculated to be −35,900 deg·cm^2·dmol^{-1} using the equation: $X_H^n = X_H^\infty(1 - k/n)$, where X_H^∞ is the molar ellipticity for a helix of infinite length and is equal to −39,500 deg·cm^2·dmol^{-1}, n is equal to 28 residues, and k is wavelength-dependent constant equal 2.57 at 222 nm.[33]

sequences since values from 69 to 96% are common for three to five heptad-repeat coiled-coils.[15,32] The fact that it is less than 100% helical likely arises from end-fraying.

The 2*c*-Os/2*b*-Ru peptide pair showed a minor destabilization when compared to the 2*f*-Os/2*f*-Ru pair. The difference in ΔG_{unfold} (8.2 ± 0.10 kcal/mol) for the 2*c*-Os/2*b*-Ru peptide pair corresponds to an increase in the extrapolated K_d (0.97 ± 0.20 μM). The maximum ellipticity for the 2*c*-Os/2*b*-Ru pair (−26,400 ± 700 deg·cm^2·dmol^{-1}) corresponds to 74% α-helicity, indicating slightly less α-helical character when compared to the 2*f*-Os/2*f*-Ru dimer. Not unexpectedly, the 2*g*-Os/2*e*-Ru peptide pair was found to be the least stable heterodimer, as this pair places the Ru(II) and Os(II) closest to the dimerization interface, although the magnitude of the destabilization was again quite minimal. The extrapolated ΔG_{unfold} (8.0 ± 0.10 kcal/mol) value for the 2*g*-Os/2*e*-Ru pair is within error of that reported for the 2*c*-Os/2*b*-Ru pair. The calculated K_d (1.4 ± 0.3 μM) value for 2*g*-Os/2*e*-Ru pair is therefore also within error. The maximum ellipticity (−25,900 ± 300 deg·cm^2·dmol^{-1}) for the 2*g*-Os/2*e*-Ru dimer corresponds to 72% α-helicity.

Although the thermodynamic parameters (ΔG_{unfold}, K_d, and % α-helicity) for the 2*b*-Ru/2*c*-Os and 2*e*-Ru/2*g*-Os metallopeptide pairs are within error, the GndHCl denaturation midpoints ($[\text{GndHCl}]_{1/2}$ = 2.0 ± 0.05 M for the 2*b*-Ru/2*c*-Os and 1.8 ± 0.05 M for the 2*e*-Ru/2*g*-Os) for the two pairs analyzed at the same total peptide concentrations are well outside of error. Chemical denaturation midpoints are often used to compare structurally similar peptide sequences since ΔG_{unfold} values are extrapolated and inherently prone to error.[31,33] The difference in free energy of unfolding between the 2*b*-Ru/2*c*-Os and 2*e*-Ru/2*g*-Os metallopeptide pairs ($\Delta\Delta G_D$) was calculated to be 0.3 kcal·mol^{-1} based on the difference between the $[\text{GndHCl}]_{1/2}$ values (see Experimental Section).[31,33]

Solubility issues prevented full analysis of the parent sequences lacking Ru(II) or Os(II) complexes by GndHCl denaturation. On the basis of the relatively small degree of destabilization within the different metallopeptide pairs, it is expected that the 2*f*-Os/2*f*-Ru pair and the parent sequences would not be measurably different. Qualitative examination of CD spectra for the parent sequences also indicated a similar folding behavior (see Supporting Information). This conclusion

dx.doi.org/10.1021/ic300669t | Inorg. Chem. 2012, 51, 11324−11338

agrees with Ogawa's studies of de novo designed electron transfer metallopeptides, where very little destabilization was measured when large transition metal complexes were attached at *f* positions within the sequence.[15] The ΔG_{unfold} and K_d values reported for the three metallopeptide dimers were similar to those reported by Ogawa,[15] and other previously reported values corresponding to four-heptad coiled-coils,[20c] taking into account that the two asparagine substitutions are expected to be slightly destabilizing.[19,20b,21]

Subsequent photophysical measurements, including the appropriate control experiments, were conducted at concentrations well above the measured K_d values.

Photophysics. *Steady-State Spectroscopy.* The ground state absorption spectrum for the 2*g*-Os/2*e*-Ru metallopeptide pair exhibits a peak at 450 nm and a lower energy band that is centered at 650 nm (Figure 6). The peak centered at 450 nm is

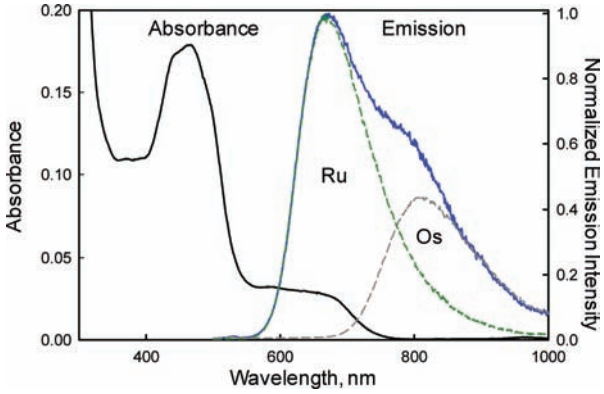

Figure 6. The UV−vis absorption (black:25 μM 2*e*-Ru and 50 μM 2 g-Os) and steady state emission (blue: 25 μM 2*e*-Ru and 50 μM 2 g-Os) spectra of the 2*g*-Os/2*e*-Ru peptide coiled-coil in a 10 mM sodium phosphate buffer solution, pH 7, 25 °C. Also shown are the 2*e*-Ru(II) peptide (green dashed: 25 μM 2*e*-Ru) and 2*g*-Os(II) peptide emission spectra (gray dashed: 100 μM 2 g-Os). The excitation wavelength was 450 nm.

the singlet metal-to-ligand charge transfer (^{1}MLCT) for both the Ru(II) and Os(II) bipyridyl complexes, while the lower energy band corresponds to direct excitation of the ^{3}MLCT in the Os(II) complex which is optically accessible because of large spin−orbit coupling. When excited at 450 nm, the steady state emission spectrum for the 2*g*-Os/2*e*-Ru peptide exhibits a higher energy band (λ_{max} at 660 nm) that corresponds to Ru(II) ^{3}MLCT emission after fast intersystem crossing from the ^{1}MLCT, while the peak centered at 800 nm is Os(II) ^{3}MLCT emission (Figure 6). The steady-state emission spectra show an increase in the Os(II) emission as the chromophores are moved closer to each other, providing direct evidence for Ru(II) to Os(II) energy transfer (see Supporting Information, Figure S3).

Time-Resolved Spectroscopy. Photoexcitation of the Ru(II) center at 450 nm is followed by rapid relaxation into the ^{3}MLCT band, and potentially triplet−triplet energy transfer to the lower energy Os(II) site. In principle, energy transfer can be observed either through the quenching of Ru(II) emission at 660 nm or the appearance of the Os(II) emission at 800 nm. In practice, however, the Os(II) emission due to energy transfer is obscured by Ru(II) emission in the low energy tail and phosphorescence arising from the direct excitation of Os(II) at 450 nm. Both these contributions make a quantitative analysis of the Os(II) emission difficult. While Ru(II) emission contaminates the emission of Os(II) at 800 nm, the converse is not true, and both the time-resolved and steady-state emission measurements show no detectable Os(II) emission at 660 nm. Thus, Ru(II) emission provides the cleanest window through which to view Ru-to-Os energy transfer.

The P1/2*e*-Ru coiled-coil was used as a control to measure the Ru lifetime in the absence of energy transfer (Figure 7a).

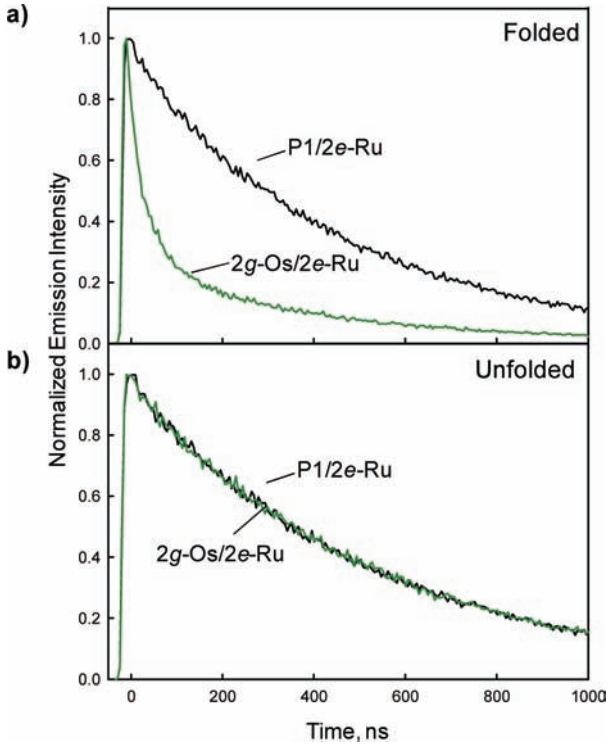

Figure 7. (a) Time-resolved emission of 2*e*-Ru peptide in the presence of the P1 peptide (black: 25 μM 2*e*-Ru and 50 μM P1) and the 2*g*-Os peptide (green: 25 μM 2*e*-Ru and 50 μM 2*g*-Os) in a 10 mM sodium phosphate buffer solution at pH 7 and 25 °C. (b) P1/2*e*-Ru peptide with chemical denaturant (black: 25 μM 2*e*-Ru, 50 μM P1 and 5 M guanidinium chloride, 20 mM sodium phosphate, and 100 mM sodium chloride buffer at pH 7 and 25 °C and 2*g*-Os/2*e*-Ru peptide pair with chemical denaturant (green: 25 μM 2*e*-Ru, 50 μM 2*g*-Os, and 5 M guanidinium chloride, 20 mM sodium phosphate, and 100 mM sodium chloride buffer at pH 7 and 25 °C). Ru(II) emission quenching by energy transfer is turned off in the presence of the chemical denaturant. The time-resolved emission data were collected at 660 nm with an excitation of 444 nm.

The decay is single exponential with a lifetime around 450 ns (2.2×10^6 s^{-1}), comparable to the lifetime of $Ru(bpy)_3^{2+}$ in water.[34] Pairing of 2*e*-Ru with the 2*g*-Os peptide instead of the unmodified P1 results in quenched Ru(II) emission due to energy transfer (Figure 7a). The decay is biexponential with a fast component of 42 ns that is related to energy transfer and a slow component that matches the Ru(II) lifetime of 450 ns. The slow component is attributed to a small fraction of unassociated Ru(II) chains in solution that are present as a result of the ground state equilibrium between the peptide chains.

Influence of Folding on Energy Transfer. A comparison of the energy transfer dynamics in the folded and unfolded state can be achieved through denaturation of the peptide scaffold, which in principle can be accomplished by either heating or

chemical additives. Temperature induced denaturation is more problematic because of the high thermal stability of the coiled-coil peptides. The analysis would be further complicated by the fact that the Ru(II) ^{3}MLCT excited state lifetime is diminished with increasing temperature because of the thermally accessible metal-centered (^{3}dd) excited states that undergo rapid nonradiative decay. Chemical denaturation with GndHCl provides a viable alternative method for studying the denatured state at the same concentration used for time-resolved experiments.

The 660 nm decays for the P1/2*e*-Ru and 2*g*-Os/2*e*-Ru systems in the presence of guanidine denaturant were measured and compared to the nondenatured complex (Figure 7b). The excited state lifetime of the 2*e*-Ru peptide is slightly longer in the highly polar 5 M GndHCl denaturation medium (τ = 520 ns compared to 450 ns in buffer), but is unaffected by the presence of up to 2 equiv (50 mM) of the 2*g*-Os peptide.

The ability of the chemical denaturant to turn off energy transfer confirms that the Ru(II) emission quenching arises from the folded coiled-coil peptide structure and not from nonspecific interactions between the peptide chains.

In addition, an Os(II) "control complex" (**4**, Figure 8) was designed to mimic the acceptor module, while lacking any

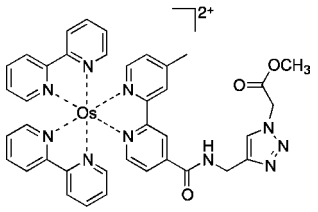

Figure 8. Os(II) complex (**4**) was used as a diagnostic for intermolecular energy transfer not mediated by the peptide scaffold.

molecular recognition elements that would allow for association with the partner peptide. When the control complex (**4**) was mixed with the 2*b*-Ru peptide, no change in the excited-state lifetime was observed with up to 2 equiv present. This differs from similar studies of Ru(II) and Os(II) modified oligonucleotides, which show that the addition of a non-covalently attached Os(II) complex ($[Os(bpy)_2(phen)]^{2+}$) to a Ru(II)-containing oligonucleotide solution results in some quenching (~8%) of the Ru(II) based phosphorescence, even at much lower Os(II) concentrations.[10c] This observation could be a consequence of the difference in the net charge on the two scaffolds or intercalation.[10e] The oligonucleotides used in that work are polyanionic molecules, and may have attractive charge−charge interactions with bipyridyl complexes that result in aggregation in solution. The 2*b*-Ru peptide on the other hand contains a net positive (+5) charge at pH 7, resulting in a repulsive charge−charge interactions with the control complex. In addition, weak intercalation of the bpy ligands into the DNA duplex may be responsible for the observed quenching in the DNA system, which is not possible in this peptide scaffold.[10e]

The results of the two control experiments clearly demonstrate that energy transfer within the peptide system occurs between coiled-coil dimer partners, and requires the folded self-assembled peptide scaffold for structural organization.

Positional Variation and Energy Transfer. We compared the Ru(II) emission quenching for the three coiled-coil metallopeptide pairs: 2*f*-Os/2*f*-Ru, 2*c*-Os/2*b*-Ru, and 2*g*-Os/2*e*-Ru (Figure 9), along with the transients from three coiled-coils containing the Ru(II) metallopeptides paired to the P1

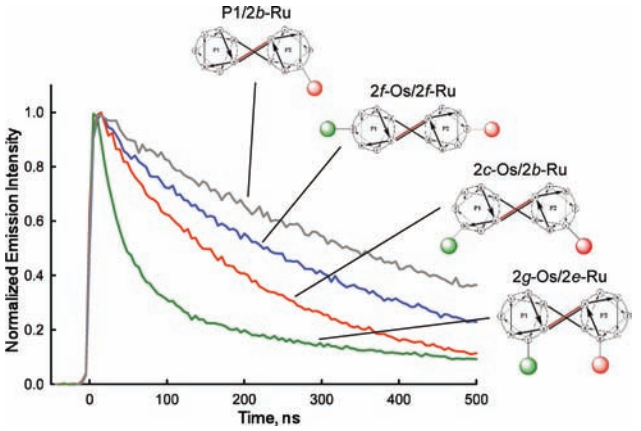

Figure 9. Time-resolved emission transients showing the distance dependence of the energy transfer rate for the 2*f*-Os/2*f*-Ru (blue: 25 μM 2*f*-Ru and 50 μM 2*f*-Os), 2*c*-Os/2*b*-Ru (red: 25 μM 2*b*-Ru and 50 μM 2*c*-Os), and 2*g*-Os/2*e*-Ru (green: 25 μM 2*e*-Ru and 50 μM 2 g-Os) peptide pairs in 10 mM phosphate buffer solution at pH 7 and 25 °C. The P1/2*e*-Ru peptide (gray: 25 μM 2*e*-Ru and 50 μM P1) is shown for comparison. From the transients it is clear that the energy transfer rate is faster the closer the metal complexes are placed to one another. The time-resolved emission data were collected at 660 nm with an excitation wavelength of 444 nm.

apopeptide. All three of the P1/Ru(II) systems exhibit qualitatively similar monoexponential decay kinetics (Table 3). Each transient in the mixed Ru(II)/Os(II) systems is

Table 3. Results of the Global Analysis Showing the Dependence of the Energy Transfer Rate on the Position[a]

	K_a, μM^{-1} (K_d, μM)	k_{Ru}, × 10^6 s^{-1} (lifetime, ns)	k_{EnT}, × 10^6 s^{-1} (lifetime, ns)
2*f*-Os/2*f*-Ru	0.908 ± 0.005 (1.101 ± 0.006)	2.9 ± 0.002 (478.7 ± 0.5)	1.0 ± 0.02 (816 ± 14)
2*c*-Os/2*b*-Ru	0.919 ± 0.001 (1.088 ± 0.002)	2.2 ± 0.002 (450.0 ± 0.5)	3.0 ± 0.02 (304 ± 2)
2*g*-Os/2*e*-Ru	0.887 ± 0.001 (1.127 ± 0.001)	2.1 ± 0.002 (468.2 ± 0.4)	23 ± 0.1 (42.0 ± 0.2)

[a]All peptide samples contained 25 μM Ru peptide and 0 to 50 μM Os peptide in 10 mM sodium phosphate buffer at pH 7 and 25 °C. The error is from the global fitting analysis.

biexponential, where the slow component arises from the free Ru chains in solution and the fast component reflects Ru quenching due to energy transfer. The peptide pair that places the complexes the farthest apart, 2*f*-Os/2*f*-Ru (Figure 9 blue line), has the largest distance between alpha carbons (14.0−14.9 Å), and results in the slowest energy transfer. The 2*g*-Os/2*e*-Ru peptide pair (Figure 9, green line) places the complexes the closest to each other with an α-carbon distance of 9.6−10.3 Å, and has the fastest energy transfer. Lastly, the 2*c*-Os/2*b*-Ru peptide pair has an intermediate spacing (12.7−13.5 Å) and its energy transfer rate falls in the middle (Figure 9, red line). The trend of the quenching rates indicates that the peptide assembly influences the relative positions of the Ru(II) and Os(II) complexes, and thus their ability to undergo energy transfer, in a predictable manner.

Data Analysis. The emission decay was measured in a series of 2*g*-Os/2*e*-Ru samples in which the 2*e*-Ru peptide

dx.doi.org/10.1021/ic300669t | *Inorg. Chem.* 2012, 51, 11324−11338

concentration is kept constant at 25 μM and the 2*g*-Os peptide concentration is incrementally increased from 0 μM to 50 μM (Figure 10). As the 2*g*-Os peptide concentration is increased

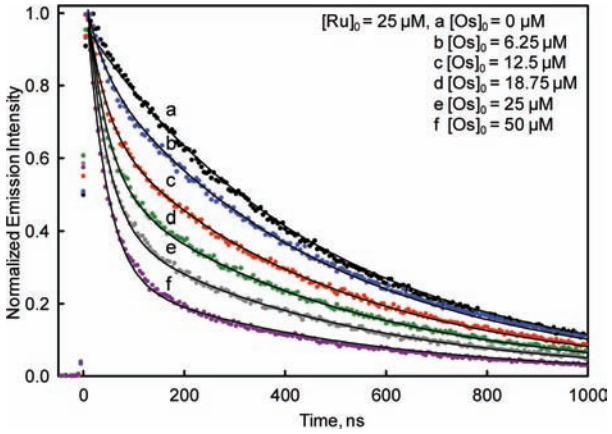

Figure 10. Time-resolved emission for P1/2*e*-Ru peptide (black: 25 μM 2*e*-Ru and 50 μM P1) and 2*g*-Os/2*e*-Ru peptide pair containing various amounts of the 2*g*-Os peptide (blue: 6.25 μM, red: 12.5 μM, green: 18.75 μM, gray: 25 μM, and purple: 50 μM with all containing 25 μM 2*e*-Ru) in a 10 mM phosphate buffer solution at pH 7 and 25 °C. The increase in 2*g*-Os peptide concentration drives the equilibrium to heterodimer formation and thus greater Ru(II) emission quenching by energy transfer. The time-resolved emission data were collected at 660 nm with an excitation wavelength of 444 nm.

the slow component decreases in amplitude, consistent with a diminishing amount of free Ru(II). The relative amplitudes of the two kinetic components reflect the fractions of Ru(II)/Os(II) dimer (fast) and free Ru(II) peptide (slow), resulting in an intensity decay that can be expressed as

$$I(t) = \left(\frac{[\mathrm{RuOs}]}{[\mathrm{Ru}]_0}\right)e^{-(k_{\mathrm{Ru}}+k_{\mathrm{EnT}})t} + \left(\frac{[\mathrm{Ru}]_0 - [\mathrm{RuOs}]}{[\mathrm{Ru}]_0}\right)e^{-k_{\mathrm{Ru}}t} \quad (1)$$

where k_{EnT} is the energy transfer rate and k_{Ru} is the rate of Ru(II) excited state decay. The relative amplitudes of the two components are dependent on the concentration of associated heterodimers, [RuOs], which is determined by the ground state equilibrium:

$$\mathrm{Ru} + \mathrm{Os} \rightleftarrows \mathrm{RuOs} \quad (2)$$

$$K_a = \frac{[\mathrm{RuOs}]}{[\mathrm{Ru}][\mathrm{Os}]} = \frac{[\mathrm{RuOs}]}{([\mathrm{Ru}]_0 - [\mathrm{RuOs}])([\mathrm{Os}]_0 - [\mathrm{RuOs}])} \quad (3)$$

where $[\mathrm{Ru}]_0$ and $[\mathrm{Os}]_0$ are the total concentrations of the two peptides and K_a is the equilibrium constant.

The solid lines in Figure 10 are the result of a global nonlinear least-squares fit of the series of decays obtained at different Os(II) concentrations to eqs 1−3 with k_{EnT}, k_{Ru}, and K_a being adjustable parameters. Table 3 summarizes the fitting results for the three peptide pairs. The 2*g*-Os/2*e*-Ru peptide pair exhibits the fastest energy transfer with $k_{\mathrm{EnT}} = 2.3 \times 10^7$ s^{-1} (42 ns) and the 2*f*-Os/2*f*-Ru peptide pair has the slowest with $k_{\mathrm{EnT}} = 1.0 \times 10^6$ s^{-1} (816 ns), and the 2*c*-Os/2*b*-Ru pair fell in the middle at 3.0×10^6 s^{-1} (304 ns). The relatively slow energy transfer times in comparison with the lifetime of the Os(II) excited state (16 ns, 6.21×10^7 s^{-1}) prevents a build-up of Os(II) excited state population. Hence a delayed rise in the Os emission, which has been observed in other systems,[6e] is not observed here. The long linker between the chromophore and the peptide scaffold will cause the attached chromophores to experience a variety of conformations that interconvert on the time scale of the excited state lifetime. Because energy transfer will be more favorable when the two chromophores are in close proximity, the observed rate will likely also reflect the time scale for structural fluctuations.

All-atom molecular dynamics simulations (discussed below) depict the bipyridyl complexes in the 2*g*-Os/2*e*-Ru and 2*c*-Os/2*b*-Ru systems in direct contact, and therefore the energy transfer occurs through Dexter energy transfer mechanism.[35] On the other hand the simulations show the complexes in the 2*f*-Os/2*f*-Ru system remaining at a significant metal−metal separation (3 nm). Therefore the energy transfer mechanism for the 2*f*-Os/2*f*-Ru system is unlikely to be through space Dexter energy transfer. Förster, energy transfer, which occurs through a dipole−dipole mechanism, can occur over larger donor−acceptor separations.[35] Although Förster energy transfer is formally forbidden for triplet−triplet energy transfer, the large spin−orbit coupling in these late transition metal complexes, particularly the Os(II), may provide it with some allowed character.[35] The presence of Förster energy transfer at longer separations is consistent with observations made in other Ru(II)/Os(II) energy transfer systems.[6e,10a−c] Regardless of the mechanism, the coiled-coil peptide system is an effective scaffold for controlling the donor/acceptor placement and hence energy transfer rate in molecular assemblies.

All-Atom Molecular Dynamics Simulations. All atom molecular dynamics simulations were performed on each of the three coiled-coils to gain insight into the molecular level interactions in these systems. Since Ru(II) and Os(II), when enveloped by the bipyridyl ligands, are practically identical from a molecular dynamics perspective, Ru(II) was used as the central atom for simulation in both bipyridyl complexes. For the sake of concise comparisons with experiments, we retain the same nomenclature for the metallopeptide pairs. It is important to mention that since a single metal−metal distance can map into a variety of different conformational arrangements between two metal complexes, we present below detailed trajectory analysis, with supplementary movies providing additional structural information (see Supporting Information).

2f-Os/2f-Ru Heterodimer. Both bipyridyl complexes in the 2*f*-Os/2*f*-Ru system start from a distal position relative to the peptide backbone. During the equilibration phase the complexes were frequently found in the proximity of the coiled-coil peptide backbone, likely driven by favorable hydrophobic interactions. To overcome the bias of the deliberately chosen initial conditions, the first 250 ns of the simulation were not included when calculating the distance distributions. The subsequent data collection phase was run for approximately 500 ns. The dynamics of the bipyridyl complexes and their unnatural side chains can be described by two regimes. First, there are large-scale conformational rearrangements during which the tethered complexes escape from their states bound to the coiled-coil and are free to explore the phase space to find new collapsed conformations. Second, there are small-scale oscillations within these conformations, which occur on a much faster time scale, but do not result in significant displacement of the metal complexes. The attachment points for the bipyridyl complexes in the 2*f*-Os/2*f*-Ru system are far enough away from each other that the two complexes do not come into direct contact during the entire course of the

dx.doi.org/10.1021/ic300669t | *Inorg. Chem.* 2012, 51, 11324−11338

simulation. The corresponding metal-center displacement distributions and the trajectories from which they were derived are shown in Figure 11. The intermetal distance distribution is

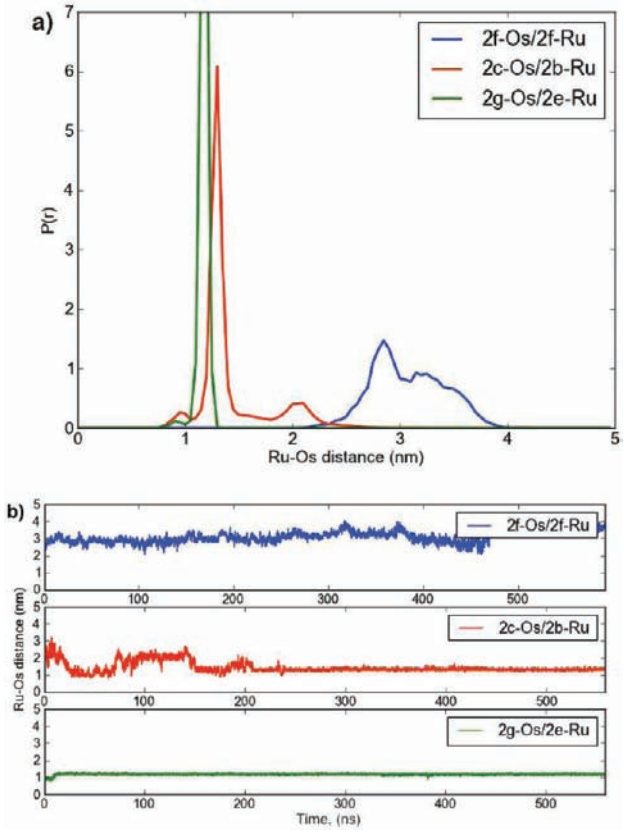

Figure 11. (a) Comparative plot of Ru−Os distance histograms (normalized) for different chromophore placements, including 2*f*-Os/2*f*-Ru, 2*c*-Os/2*b*-Ru, and 2*g*-Os/2*e*-Ru. (b) Ru−Os distance evolution in time for the 2*f*-Os/2*f*-Ru, 2*c*-Os/2*b*-Ru, and 2*g*-Os/2*e*-Ru metallopeptide pairs.

broad (over a 3 nm range) and non-Gaussian. Throughout the course of the simulation, the metal-center displacements observed for the 2*f*-Os/2*f*-Ru system are relatively large and would be expected to limit the efficiency of energy transfer. As discussed above, these simulations indicate that the Förster energy transfer mechanism may play an important role for this complex.

Interestingly, the bipyridyl complexes appear to influence the stability of the 2*f*-Os/2*f*-Ru coiled-coil structure as illustrated in the Supporting Information, Movie 6. α-Helical peptides have an increased propensity toward fraying near the termini, and when the metal complex and the 2*f*-Os/2*f*-Ru peptide terminus approach each other, the complex can entrain the ends of the peptides by providing competing hydrophobic interactions which result in further fraying. This partial folding and unfolding can be observed in the timeline plot of the helicity index α which is equal to the ratio of the number of residues in the α-helical conformation compared to the total number of residues in a sequence (see Figure 12 and Table 4). The implications of this observation are elaborated below.

2c-Os/2b-Ru Heterodimer. After extensive equilibration for approximately 300 ns, the initial conformation for the data collection corresponded to spatially separated bipyridyl complexes with relaxed linkers and a slightly perturbed

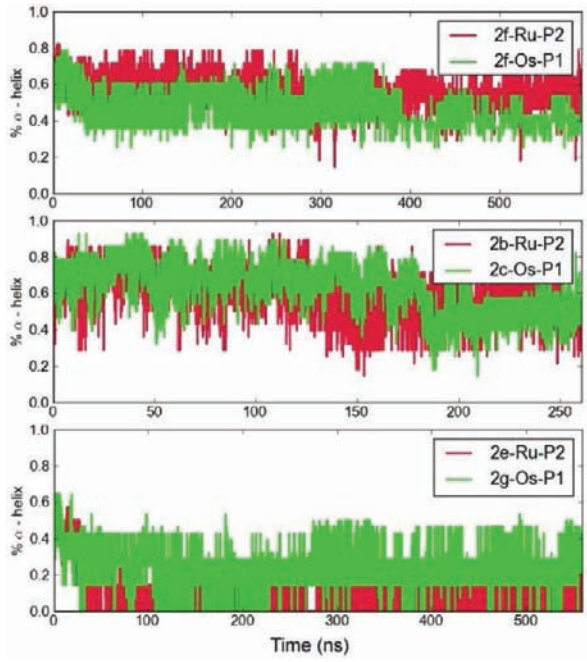

Figure 12. Fraction of α-helical content in each peptide as a function of time shown for the 2*f*-Os/2*f*-Ru (top), 2*c*-Os/2*b*-Ru (middle), and 2*g*-Os/2*e*-Ru (bottom) metallopeptide pairs. Each peptide actively explores its conformational space, while predominantly staying in an α-helical state. The exception is 2*g*-Os/2*e*-Ru system (see bottom graph), where an unfolding event is caught during MD. Visualization of the trajectory showed that peptide termini started interacting with the bipyridyl complexes and significantly disrupted the overall coiled-coil ternary and secondary structure.

Table 4. Dependence of the Coiled-Coil Secondary Structure and Metal-Center Displacement on Substitution Position

	helicity index α, X-*Os*-*P1*	helicity index α, Y-*Ru*-*P2*	*Ru*−*Os* average distance
X = 2*f*, Y = 2*f*	0.458 ± 0.097	0.559 ± 0.079	3.100 ± 0.336
X = 2*c*, Y = 2*b*	0.631 ± 0.139	0.593 ± 0.124	1.444 ± 0.319
X = 2*g*, Y = 2*e*	0.249 ± 0.097	0.070 ± 0.116	1.195 ± 0.048

structure for the coiled-coil scaffold. During the first 20 ns of the production run, the bipyridyl complexes do not form any stable close contact, with one complex actively exploring the surface of the peptide scaffold. At ∼25 ns the two complexes contact each other and form a loose association, in which a single bipyridyl ring aligns with the triazole ring of the complementary peptide linker (see Figure 13c). This was followed by close packing of the metal complexes, and resulted in $\pi-\pi$ stacking of bipyridine rings (see Figure 13b). The metal complexes showed relatively fast (∼0.2 ns) conformational rearrangement of the bipyridine rings between them, often including a non-parallel, ∼45° metastable $\pi-\pi$ stacking (see Supporting Information, Movies 1 and 2).

The comparative graph of distance distributions in Figure 11 shows that 2*c*-Os/2*b*-Ru system has three main peaks dominated by the close-packed geometry at less than 1.5 nm. The timeline of Ru−Os distance has a feature of switching from one basin with more closely $\pi-\pi$ stacked state(s), in which bipyridine rings align in a mostly parallel fashion (Figure 13b), to another, where the complexes are in close proximity to one

dx.doi.org/10.1021/ic300669t | *Inorg. Chem.* 2012, 51, 11324−11338

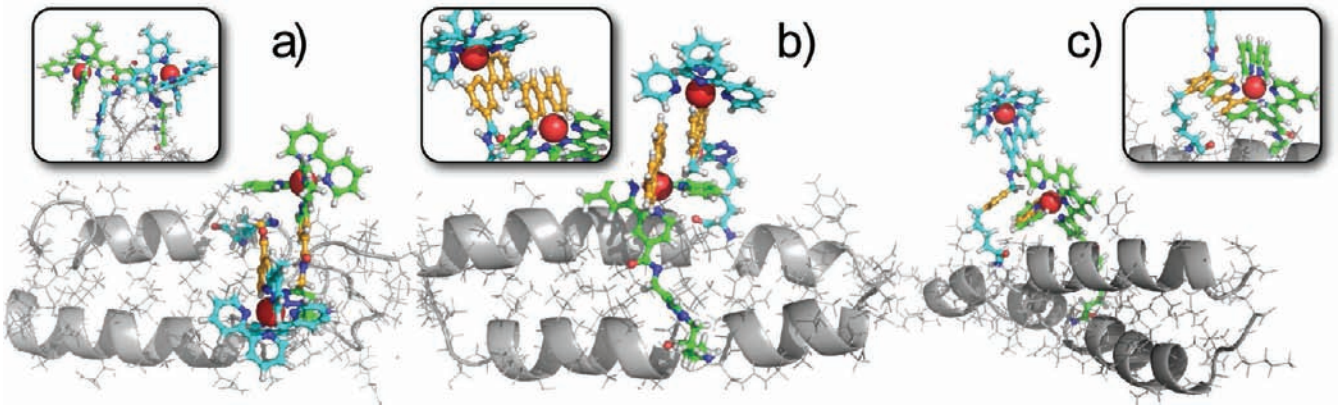

Figure 13. (a) Bipyridyl ligands arranged in a "neck" conformation, facing away from each other (1.2 nm feature). This conformation was only observed in the 2*g*-Os/2*e*-Ru system. (b) $\pi-\pi$ stacking arrangement where bipyridyl rings of two complexes are in van der Waals contact and parallel to each other (~1 nm feature). In our simulations $\pi-\pi$ stacking was often shifted and was not stable for longer than ~10 ps. This tightly stacked conformation is observed consistently in 2*c*-Os/2*b*-Ru system and briefly in 2*g*-Os/2*e*-Ru system. (c) "Loose" packing arrangement of the bipyridyl complexes (~2 nm feature) is a stable basin of conformations with characteristic $\pi-\pi$ stacking of one of bipyridine rings of one chromophore and the triazole ring on the linker of the other. This stacking is stable in 2*c*-Os/2*b*-Ru system and transitory to closer intercomplex packing conformations in 2*g*-Os/2*e*-Ru system.

another, yet not in direct contact. These conformations correspond to the 2*c*-Os bipyridine ring $\pi-\pi$ stacking with the triazole ring of 2*b*-Ru linker, as shown in Figure 13c. However the contribution from loose packing conformations is statistically larger, as can be illustrated by comparing the heights of the first peak at < 1 nm ($\pi-\pi$ stacking, see Figure 13b) and the second peak at approximately 1.2 nm (loose packing, see Figure 13c) in the Figure 11a.

In this system, we did not observe a similar perturbation of the peptide scaffold by the bipyridyl complexes as was seen in the 2*f*-Os/2*f*-Ru system. The peptide termini dynamically unfold and refold during the course of simulations (see Supporting Information, Movies 2 and 3), but not because of association with the bipyridyl complexes in this case. The helicity index of the 2*c*-Os-P1 and 2*b*-Ru-P2 peptides is shown in Figure 12. Interestingly, the standard deviation of the helicity index is approximately 2-fold higher for the 2*c*-Os/2*b*-Ru system, indicating that peptides are more dynamic and actively explore their phase space (see Table 4).

2g-Os/2e-Ru Heterodimer. In a manner very similar to the two previous systems, the bipyridyl complexes in the 2*g*-Os/2*e*-Ru system quickly collapsed onto the coiled-coil peptide scaffold during the equilibration phase ~250 ns. The two metal complexes came into van der Waals contact with each other in a conformation very similar to the intermediate chromophore packing arrangement that was observed in the 2*c*-Os/2*b*-Ru system (Figure 13c). For 30 ns the bipyridyl complexes fluctuate between the $\pi-\pi$ stacking (see Figure 13b) and looser ligand arrangements, as shown in Figure 11b. Finally, we observe one more major conformational rearrangement where a tight "neck" stacking is achieved, which is characterized by the bipyridyl ring and a part of the connected linker of one complex aligning with the corresponding structural parts of the other. As a result, the complexess are facing away from each other (see Figure 13a and Supporting Information, Movie 4). This conformation, which was not observed in the 2*c*-Os/2*b*-Ru system, persists until the end of the simulation. As shown in Figure 13a and Supporting Information, Movie 5, the bipyridyl complexes in the 2*g*-Os/2*e*-Ru system also maintain a close proximity with the bipyridyl ligands spending most of their time in van der Waals contact.

This "neck" stacking creates a significant amount of strain for the peptide scaffold, as well as an additional hydrophobic surface consisting of the linker side chains pulled together. We show in Figure 13a and Supporting Information, Movie 5 that the peptide termini closest to the bipyridyl complex detach from the coiled-coil interface and bind to the groove between linkers or wrap around the bipyridyl complexes themselves, leading to more disruption of the coiled-coil structure, compared with the other two systems (see Figure 13). The analyses of the simulation data for all three systems suggest that the various placements of the complexes results in dissimilar complex-peptide interactions, where the latter influence the corresponding coiled-coil stabilities (see Table 4). Furthermore, although the trends predicted from the MD simulations are qualitatively consistent with the corresponding thermodynamic measurements, the quantitative extents of the coiled-coil disruption seen in simulations are likely overestimated. The following possibilities could have contributed to producing extra fraying in our MD simulations: (1) overestimating the metal-complex-peptide interactions, (2) underestimating the strength of the interpeptide bonding, or (3) preparing the initial coiled-coil conformations in an imperfect way, which did not allow tight enough packing of side-chains or accurate enough alignment of hydrophobic interactions (see the Experimental Section).

In summary, comparison of the dynamics for all three metallopeptide systems shows that the 2*g*-Os/2*e*-Ru pair has the narrowest Ru(II) to Os(II) distance distribution with the smallest probable separation (~1 nm), and would therefore be the best promoter for energy transfer. A metal−metal distance of 1 nm suggests that the complexes are in close contact with each other and would imply efficient energy transfer, regardless of which mechanism is considered. This is in agreement with the photophysical measurements made on the metallopeptide systems, which also indicated the 2*g*-Os/2*e*-Ru pair to be the most efficient energy transfer promoter, as discussed above. Importantly, we have not observed unfolding of the coiled-coil near the linker attachment points for any of the three systems. This suggests that the dynamics of the bipyridyl complexes themselves do not impose a significant stress along the peptide backbone in our scaffold design. To gain deeper insights into

dx.doi.org/10.1021/ic300669t | *Inorg. Chem.* 2012, 51, 11324−11338

the mechanisms of energy transfer in these systems, subsequent quantum mechanical calculations can be carried out on selected structural snapshots of stable stacking conformations observed in the MD simulations. This, in turn, may help to improve the design of peptide scaffolds, allowing for more precise control over molecular components.

III. CONCLUSIONS

The ability to control the positioning and organization of molecular components is central to the design of functional molecular-based materials.[3] However, architectures that rely solely on covalent bonding for structure (e.g., polymers, dendrimers) have limited control over the assembly geometry and higher-order spatial control. Using peptides as scaffolds, we have designed an artificial self-assembling system that utilizes weak forces to control the relative placement of Ru(II) and Os(II) complexes. The assemblies incorporate an α-helical coiled-coil peptide scaffold consisting of α-helical heterodimers in which each coil is functionalized with either a Ru(II)-containing energy donor or with an Os(II)-containing energy acceptor. This architecture differs from many other types of molecular assemblies in that it uses both intra- and intermolecular noncovalent interactions to adopt well-defined secondary and tertiary structures that control the placement of the energy transfer complexes. Moreover, the use of "click" chemistry allows for straightforward and well-defined control of the placement of the covalently linked chromophores.

Circular dichroism spectroscopy in conjunction with time-resolved emission spectroscopy confirms the importance of the heterodimeric α-helical coiled-coil structure for modulating energy transfer. Ru(II) to Os(II) energy transfer is only observed in the folded structures, and energy transfer rates measured across a series of supramolecular structures are consistent with a systematic variation of the metal complex separation. Chemical agents that denature the peptide scaffold also serve as an on-off switch, and completely disable energy transfer. Molecular dynamics simulations show Ru(II)−Os(II) distance distributions that are consistent with the order of the experimentally measured energy transfer rates. In addition, the simulations suggest that the assemblies maintain their α-helical character, but are dynamic in nature, with stable cores but multiple conformations interchanging on the nanosecond time scale. These studies demonstrate the sequence-structure-function paradigm found in natural proteins in a robust artificial self-assembling system and clearly establishes the essential role the supramolecular scaffold plays in controlling function. This system provides a promising new scaffold for functional materials that couples straightforward synthesis with fine control of three-dimensional structure that directly dictates function.

IV. EXPERIMENTAL SECTION

General Methods. Solvents were purchased from Fisher Scientific and were used as received unless noted otherwise. *cis*-Dichlorobis(2,2′-bipyridine)ruthenium(II) dihydrate was purchased from Strem Chemicals. All α-N-Fmoc-amino acids, including α-N-Fmoc-lysine, were purchased from Novabiochem. Tetrakis(acetonitrile)copper(I) hexafluorophosphate, 2,2′-bipyridine, 4,4′-dimethyl-2,2′-bipyridine, and tripropargylamine were purchased from Aldrich. The compounds 4′-methyl-2,2′-bipyridine-4-carboxaldehyde, 4′-methyl-2,2′-bipyridine-4-carboxylic acid, and succinimidyl-4-carboxy-4′-methyl-2,2′-bipyridine were synthesized according to reported procedures.[36] *cis*-Dichlorobis-(2,2′-bipyridine)osmium(II) was synthesized using the procedure reported by Meyer.[37] Deuterated solvents were purchased from Cambridge Isotope Laboratories. ^{1}H and ^{13}C NMR spectra were recorded at 400 and 100 MHz, respectively, on Bruker spectrometers. Chemical shifts were given in ppm relative to solvent peaks corresponding to residual protons for the deuterated solvents. These values were taken as δ 7.27, 1.93, and 5.32 for $CDCl_3$, CD_3CN, and CD_2Cl_2, respectively. Coupling constants are given in hertz. The details for peptide synthesis and purification are provided below. High-resolution and low-resolution mass spectra were obtained using a Bruker Biotof instrument. Milli-Q water was used for the preparation of all buffers and solutions.

Peptide Synthesis. Peptides were synthesized by standard automated SPPS using a Thuramed tetras synthesizer. Fmoc-protected amino acids were used along with a CLEAR-Amide resin from Peptides International, Inc. Amino acid residues were activated with HBTU, HOBt, and DIPEA in DMF. Amino acids were deprotected twice with 2% DBU and 2% piperidine in DMF for 15 min each step. Commercially available amino acids were coupled using double coupling cycles of 30−60 min each. The N-terminus of each peptide was acetylated using 5% acetic anhydride and 6% lutidine in DMF for 30 min. Cleavage of the peptides from the resin was performed in 95.0% TFA, 2.5% water, and 2.5% TIPS. TFA was evaporated with a stream of nitrogen and diethyl ether was added to precipitate the cleavage products. The peptides were extracted with water or collected as solids by centrifugation and lyophilized to dryness. Peptides were purified by RP-HPLC using an Atlantis Prep OBD dC-18 semi-preparative column, with a gradient of 0−100% solvent B over 40 min, where solvent A was 95:5 water/ACN, 0.1% TFA, and solvent B was 95:5 ACN/water, 0.1% TFA. Purified samples were lyophilized and the peptide sequence was confirmed by ESI-MS. M was calculated as 3212.73 (exact) for the **P1** parent sequence ($C_{142}H_{237}N_{37}O_{47}$). MS m/z observed: 1608.4 ($[M + 2H^+]^{2+}$), 1072.6 ($[M + 3H^+]^{3+}$), 804.7 ($[M + 4H^+]^{4+}$); M was calculated as 3363.95 (exact) for the **P2** parent sequence ($C_{149}H_{258}N_{46}O_{42}$). MS m/z observed: 1123.0 ($[M + 3H^+]^{3+}$), 842.5 ($[M + 4H^+]^{4+}$), 674.0 ($[M + 5H^+]^{5+}$).

Azidopeptide Synthesis. Peptides containing azidolysine residues at desired positions were synthesized using an automated synthesizer as described above. α-Fmoc-ε-azido-*l*-lysine **2** was synthesized by the reported procedure.[18f,27] α-Fmoc-ε-azido-L-lysine **2** was injected manually, and a single 3 h coupling reaction was performed. The azidopeptides were cleaved from the resin, and purified in a fashion identical to the parent sequences. Azidopeptide identities were confirmed by ESI-MS. M was calculated as 3238.76 (exact) for **2*f*-N$_3$-P1** ($C_{143}H_{239}N_{39}O_{46}$). MS m/z observed: 1620.9 ($[M + 2H^+]^{2+}$), 1081.0 ($[M + 3H^+]^{3+}$), 811.0 ($[M + 4H^+]^{4+}$); M was calculated as 3295.78 (exact) for **2*c*-N$_3$-P1** ($C_{145}H_{242}N_{40}O_{47}$). MS m/z observed: 1649.3 ($[M + 2H^+]^{2+}$), 1099.9 ($[M + 3H^+]^{3+}$), 825.2 ($[M + 4H^+]^{4+}$); M was calculated as 3237.77 (exact) for **2*g*-N$_3$-P1** ($C_{143}H_{240}N_{40}O_{45}$). MS m/z observed: 1620.3 ($[M + 2H^+]^{2+}$), 1080.6 ($[M + 3H^+]^{3+}$), 810.7 ($[M + 4H^+]^{4+}$); M was calculated as 3389.97 (exact) for **2*f*-N$_3$-P2** ($C_{150}H_{260}N_{48}O_{41}$). MS m/z observed: 1131.0 ($[M + 3H^+]^{3+}$), 848.5 ($[M + 4H^+]^{4+}$), 679.1 ($[M + 5H^+]^{5+}$); M was calculated as 3447.00 (exact) for **2*b*-N$_3$-P2** ($C_{152}H_{263}N_{49}O_{42}$). MS m/z observed: 1150.3 ($[M + 3H^+]^{3+}$), 863.0 ($[M + 4H^+]^{4+}$), 690.6 ($[M + 5H^+]^{5+}$); M was calculated as 3389.94 (exact) for **2*e*-N$_3$-P2** ($C_{149}H_{256}N_{48}O_{42}$). MS m/z observed: 1131.0 ($[M + 3H^+]^{3+}$), 848.5 ($[M + 4H^+]^{4+}$), 679.0 ($[M + 5H^+]^{5+}$).

Metallopeptide Synthesis. In a typical procedure 8−15 mg (~2−4 μmol) of azidopeptide would be partially dissolved in 1−3 mL of 50% (v/v) DMF in 10 mM sodium phosphate buffer, pH 8.5, that was deoxygenated with N_2 for 30 min. The azidopeptide was reacted with (2 equiv) of either the Ru(II) complex **1a** or the Os(II) complex **1b** in the presence of tetrakis(acetonitrile)copper(I) hexafluorophosphate (2 equiv), and tris-(triazolylmethyl)amine ligand (**3**, 1 equiv). The mixtures were allowed to stir overnight for 12−48 h, and then diluted with water (10 mL). The aqueous solutions were frozen and lyophilized. The fully lyophilized residue was dissolved in 0.1 M aqueous TFA and passed through a Pierce polyacrylamide desalting column. The conjugates traveled through the size-exclusion media more quickly than **1a** or **1b**, and provided the final metallopeptides after purification by reversed-phase HPLC using the conditions listed

above. Metallopeptide identities were confirmed by ESI-MS. M^{2+} was calculated as 3993.96 (exact) for **2*f*-Os-P1** ($C_{178}H_{268}N_{46}O_{47}Os$). MS m/z observed: 1997.0 ($[M^{2+}]^{2+}$), 1331.8 ($[M^{2+} + H^+]^{3+}$), 999.0 ($[M^{2+} + 2H^+]^{4+}$), 799.4 ($[M^{2+} + 3H^+]^{5+}$), 666.4 ($[M^{2+} + 4H^+]^{6+}$); M^{2+} was calculated as 4050.98 (exact) for **2*c*-Os-P1** ($C_{180}H_{271}N_{47}O_{48}Os$). MS m/z observed: 2025.8 ($[M^{2+}]^{2+}$), 1350.7 ($[M^{2+} + H^+]^{3+}$), 1013.2 ($[M^{2+} + 2H^+]^{4+}$), 810.8 ($[M^{2+} + 3H^+]^{5+}$), 679.5 ($[M^{2+} + 4H^+]^{6+}$); M^{2+} was calculated as 3992.98 (exact) for **2*g*-Os-P1** ($C_{178}H_{269}N_{47}O_{46}Os$). MS m/z observed: 1996.5 ($[M^{2+}]$), 1131.3 ($[M^{2+} + H^+]^{3+}$), 998.7 ($[M^{2+} + 2H^+]^{4+}$), 799.2 ($[M^{2+} + 3H^+]^{5+}$), 666.2 ($[M^{2+} + 4H^+]^{4+}$); M^{2+} was calculated as 4055.12 (exact) for **2*f*-Ru-P2** ($C_{185}H_{289}N_{55}O_{42}Ru$). MS m/z observed: 1352.0 ($[M^{2+} + H^+]^{3+}$), 1014.1 ($[M^{2+} + 2H^+]^{4+}$), 811.6 ($[M^{2+} + 3H^+]^{5+}$), 676.5 ($[M^{2+} + 4H^+]^{6+}$), 580.0 ($[M^{2+} + 5H^+]^{7+}$); M^{2+} was calculated as 4112.14 (exact) for **2*b*-Ru-P2** ($C_{187}H_{292}N_{56}O_{43}Ru$); MS m/z observed: 1371.7 ($[M^{2+} + H^+]^{3+}$), 1029.0 ($[M^{2+} + 2H^+]^{4+}$), 823.6 ($[M^{2+} + 3H^+]^{5+}$); M^{2+} was calculated as 4055.09 (exact) for **2*e*-Ru-P2** ($C_{184}H_{285}N_{55}O_{43}Ru$). MS m/z observed: 1352.6 ($[M^{2+} + H^+]^{3+}$), 1014.5 ($[M^{2+} + 2H^+]^{+4}$).

Compound ***1a***. The propargyl amide derivatized Ru(II) complex was prepared according to the procedure reported by Khan and Grinstaff.[25a]

Compound ***1b***. The propargyl amide derivatized Os(II) complex was prepared according to the procedure reported by Khan and Grinstaff.[25a] A small round-bottom, equipped with a condenser, was charged with *cis*-dichlorobis(2,2′-bipyridine)osmium(II) (39.7 mg, 0.069 mmol), and 4′-methyl-2,2′-bipyridine-4-propargylamide (19.1 mg, 0.076 mmol, 1.1 equiv). The reagents were heated at reflux in 50% aqueous EtOH for 24 h, and then concentrated under vacuum. The residue was suspended in H_2O (100 mL), and filtered to remove unreacted *cis*-dichlorobis(2,2′-bipyridine)osmium(II). The aqueous filtrate was washed with DCM (2 × 100 mL). A portion of saturated NH_4PF_6 was added to the aqueous solution and a green precipitate formed. The precipitate was extracted into EtOAc and then concentrated to a solid under vacuum. The solid was partially dissolved in DCM, filtered, and then concentrated to provide the product as a dark green solid (18.4 mg, 26%). ^{1}H NMR (400 MHz, CD_2Cl_2): δ 8.80 (d, J = 1.2 Hz, 1H), δ 8.48 (s, 1H), δ 8.43−8.40 (m, 4H), δ 7.90−7.84 (m, 4H), δ 7.78 (t, J = 5.6 Hz, 1H), δ 7.70−7.65 (m, 4H), δ 7.63−7.59 (m, 4H), δ 7.41−7.34 (m, 4H), δ 7.44−7.41 (m, 4H), δ 7.21 (dd, J = 5.8, 1.0 Hz, 1H), δ 4.20 (dd, J = 5.6, 2.4 Hz, 2H), δ 2.69 (s, 3H), δ 2.28 (t, J = 2.4 Hz, 1H); UV−vis (CH_3CN) λ_{max} (ε): 247 (22,000), 291 (50,000), 485 (10,000), 593 (3,000); High-resolution ESI-MS: m/z calculated for $C_{35}H_{29}N_7OOs$ (M^{2+}), 337.6024; found 337.5952.

Compound ***3***. The *tris*-(triazolylmethyl)amine ligand was prepared according to the procedure reported by Chan and Fokin.[28a,c] A solution of tripropargylamine (233.0 mg, 1.777 mmol), methyl azidoacetate (805.4 mg, 6.998 mmol, 3.94 equiv), and tetrakis-(acetonitrile)copper(I) hexafluorophosphate (21.9 mg, 58.8 μmol), and DIPEA (1 mL, 5.741 mmol, ∼3 equiv to alkyne) in ACN (4 mL) was stirred under N_2 for 24 h. The reaction warmed considerably when DIPEA was added and was cooled in an ice bath. The reaction was concentrated in vacuo, and the residue was suspended in saturated aqueous $NaHCO_3$ (50 mL), extracted with CH_2Cl_2 (3 × 50 mL), dried over anhydrous Na_2SO_4, filtered, and concentrated. The product (**3**) was obtained as an off white solid after chromatography on silica gel using 5% (v/v) MeOH in CH_2Cl_2. Yield, 701 mg (83%). ^{1}H NMR (400 MHz, $CDCl_3$): δ 7.84 (s, 1H), δ 5.18 (s, 2H), δ 3.79 (s, 2H), δ 3.78 (s, 3H); ^{13}C NMR (100 MHz, $CDCl_3$) δ 166.8, 144.6, 125.2, 52.9, 50.7, 47.4. High-resolution ESI-MS: m/z calculated for $C_{18}H_{24}N_{10}O_6$ (M + Cs^+), 609.0935; found 609.0920.

Compound ***4***. A solution of **1b** (6.95 mgs, 8 μmol), methyl azidoacetate (1.42 mg, 10 μmol, 1.7 equiv), and DIPEA (3 μL) in ACN (1.5 mL) was stirred in a round-bottom and cooled in an ice bath before tetrakis (acetonitrile)copper(I) hexafluorophosphate (0.56 mgs, 1.5 μmol, 20 mol %) was added. The solution was allowed to warm to room temperature slowly and stirred for 2 days under an inert atmosphere. The Os(II) complex was purified by RP-HPLC using methods identical to those described below for the metallopeptides. ESI-MS: m/z calculated for $C_{38}H_{34}N_{10}O_3Os$ (M^{2+}), 435.12; found 435.1.

Circular Dichroism. CD spectra were recorded on a chirascan circular dichroism spectrometer. CD spectra were recorded from 185 to 260 nm using 10 mM sodium phosphate buffer, pH 7. CD spectra taken for guanidinium denaturation experiments were taken from 200 to 260 nm. All spectra were recorded at 25 °C with an optical path length of 0.1 cm. The results are expressed as the mean molar residue ellipticity $[\theta]$ with the units of degrees·cm^2·dmol^{-1} and calculated as shown in eq 4:

$$[\theta] = \theta_{obs}/(10 \times l \times c \times n) \quad (4)$$

where θ_{obs} is the observed ellipticity in millidegrees, l is the optical path length in cm, c is the molar concentration of the peptide, and n is the number of residues for the peptide.

Guanidinium Chloride Denaturations. The GndHCl denaturation experiments were conducted by monitoring the ellipticity at 222 nm as a function of GndHCl concentration. Samples were prepared from stock peptide solutions, buffer (10 mM sodium phosphate, 100 mM sodium chloride, pH 7), and a solution of 8 M GndHCl in same buffer .

GndHCl denaturation curves were analyzed using a two-state folding/unfolding model. The fraction folded (F_F) was calculated using eq 5:

$$F_F = ([\theta] - [\theta]_D)/([\theta]_F - [\theta]_D) \quad (5)$$

where $[\theta]$ is the observed molar ellipticity (eq 4), $[\theta]_F$ is the molar ellipticity of the fully folded state, and $[\theta]_D$ is the molar ellipticity of the denatured state. The fraction unfolded (F_U) was calculated using eq 6:

$$F_U = 1 - F_F \quad (6)$$

The free energy of unfolding was calculated using eq 7:

$$\Delta G = -RT\ \mathrm{Ln}(2P_T F_U{}^2/F_F) \quad (7)$$

where R is the molar gas constant, T is the temperature in Kelvin, and P_T is the total peptide concentration. The free energy of unfolding was then calculated via the method of linear extrapolation using eq 8:[20c,31]

$$\Delta G = \Delta G_{unfold} - m[\mathrm{GndHCl}] \quad (8)$$

where the points used for extrapolation were taken through the midpoint in the most linear portion of the denaturation curves. Dissociation constants (K_d) for all three metallopeptide pairs were determined using the ΔG_{unfold} values and eq 9:

$$K_d = \exp(\Delta G_{unfold}/RT) \times 10^6 \quad (9)$$

The difference in free energy of unfolding between the 2*c*-Os/2*b*-Ru and 2*g*-Os/2*e*-Ru metallopeptide pairs ($\Delta\Delta G_D$) was calculated based on the difference between their $[\mathrm{GndHCl}]_{1/2}$ values using eq 10:[8]

$$\Delta\Delta G_D = ([\mathrm{GndHCl}]_{1/2}{}^A - [\mathrm{GndHCl}]_{1/2}{}^B)(m_A + m_B)(0.5) \quad (10)$$

where $[\mathrm{GndHCl}]_{1/2}{}^A$ and $[\mathrm{GndHCl}]_{1/2}{}^B$ are the GndHCl denaturation midpoints for two metallopeptide pairs, and m_A and m_B are the slope values from eq 8 applied to the Os/2*b*-Ru and 2*g*-Os/2*e*-Ru metallopeptide pairs, respectively.

Time-Resolved Emission. Ground state absorbance measurements were conducted with a Hewlett-Packard 8453 UV−vis−NIR absorption spectrophotometer. Steady state emission (SSE) data were collected using an Edinburgh Instruments FLS920 equipped with a 450 W xenon lamp and photomultiplier tube (Hamamatsu 2658P). SSE data were collected using a bandwidth no larger than 4.0 nm and, once collected, were corrected for the emission spectrophotometer's spectral response. The FLS920 was also used for time-resolved measurements by the time-correlated single photon counting (TCSPC) technique with an instrument response of <100 ps, using a 444.2 nm diode laser (Edinburgh Instruments EPL-445, 73 ps fwhm

dx.doi.org/10.1021/ic300669t | *Inorg. Chem.* 2012, 51, 11324−11338

pulsewidth) operated at 200 kHz. A 495 nm long pass color filter was used for emission experiments.

The samples were placed in a 2.0 mm cuvette and placed at 45 degree angle from the incident laser beam. Samples were purged in Argon for >25 min just prior to emission experiments. All experiments were performed with $Abs_{444\ nm} < 0.2$ OD. The solvent for each sample was 10 μM phosphate buffer at pH 7.

Molecular Dynamic Modeling. Since no crystal structure was available for the system, the initial structure was generated using PyMOL,[38] which is a molecular visualization tool capable of constructing simple peptides. The P1 and P2 peptides were initially generated independently using PyMOL's helical parameters and were then manually aligned with care taken to avoid steric clashes and satisfy the hydrophobic interface. The ε-triazolo-L-lysine linker segment was constructed using Gaussview, part of the Gaussian 03 suite.[39] Ruthenium(II) and osmium(II) are very similar from an MD perspective. Since the primary focus of these simulations is peptide dynamics, ruthenium was used as the central atom in both complexes and osmium was not explicitly included. This is not expected to have any significant impact on the simulations, since the metal atoms are nearly completely shielded from the rest of the system by the bipyridyl ligands, and metal's formal charge, which is the sane for Ru(II) and Os(II), plays the most important role. To examine the effect of linker positioning on the compelexes, the following three systems were created: System 1, which corresponds to the 2*f*-Os/2*f*-Ru metallopeptide pair, System 2 which corresponds to the 2*c*-Os/2*b*-Ru metallopeptide pair, and System 3 which corresponds to the 2*g*-Os/2*e*-Ru metallopeptide pair.

The simulations were prepared using the AMBER[40] force field with the ff99SB[41] parameter set. Since the AMBER libraries do not possess parameters for the artificial amino acids used as tethers, or for the chromophores themselves, these values needed to be collected from literature or obtained through quantum calculations. Partial charges for the linker and chromophores were obtained from Gaussian calculations using restricted B3LYP[42] with the LANL2DZ[43] basis set. Charges derived using the restricted electrostatic potential (RESP) technique[44] gave spurious results for ruthenium and the chelating nitrogen atoms in the bipyridyl ligands. RESP has difficulty predicting the correct charge for buried atoms since the charges are assigned in an effort to reproduce the external electrostatic potential.[44] Because of this, Mulliken charges were used in lieu of RESP charges. In general, Mulliken charges tend to be slightly more exaggerated than RESP charges with an average difference in predicted charge of $0.1(\pm 0.1)\mathbf{e}$ for all atoms excluding the ruthenium and those atoms immediately surrounding it. There was insufficient memory to compute partial charges for the entire linker and complex. To deal with this issue, the partial charges for the base of the peptide up to the γ-carbon of the side chain were extracted from the standard lysine amino acid residue. Force constants for Ru−N stretches, N−Ru−N (*cis*/*trans*) bends, C−C−N−Ru dihedrals, H−C−N−Ru dihedrals and van der Waals parameters were obtained from Brandt et al.[45] Since AMBER does not explicitly support Octahedral geometry, chelating nitrogen atoms were divided into three distinctly named but chemically identical types to establish different bending force constants for cis and trans positions. Each of the three simulations were performed with ∼13000 explicit TIP3P water molecules in a box with the dimensions $\sim 75 \times 75 \times 75$ Å under periodic boundary conditions. The charge of each system was neutralized by the addition of sodium counterions, followed by the subsequent introduction of an additional 10 mM NaCl. Each system was held at constant volume, and the peptides were frozen in place while the water and ions were minimized for 200,000 steps. Subsequently, all constraints were removed from the systems, and they were minimized for an additional 200,000 steps. The systems were gradually heated via Langevin temperature control to 300 K in incremental steps of 5 K every 50 ps. The production runs proceeded under the constant pressure, moderated by Langevin piston (set to 1 atm), with 2 fs time steps using the SHAKE algorithm and Ewald summation for long-range interactions. Short-range nonbonded interactions were calculated at each step, long-range interactions were only calculated on even steps, and the pair list was updated every 10 steps. System coordinates were saved every 2000 steps (4 ps) for analysis for a total simulation length of 300 ns for each system.

■ ASSOCIATED CONTENT

Supporting Information

Figures containing the continuous variation experiments, additional circular dichroism spectra, denaturation of parent sequence, additional time-resolved emission transients, NMR spectra, and the complete ref 39 and 40. This material is available free of charge via the Internet at http://pubs.acs.org.

■ AUTHOR INFORMATION

Corresponding Author

*E-mail: mlwaters@email.unc.edu (M.L.W.), john_papanikolas@unc.edu (J.M.P.), gpapoian@umd.edu (G.A.P.).

Notes

The authors declare no competing financial interest.

■ ACKNOWLEDGMENTS

This material is based upon work wholly supported as part of the UNC EFRC: Center for Solar Fuels, an Energy Frontier Research Center funded by the U.S. Department of Energy, Office of Science, Office of Basic Energy Sciences under Award Number DE-SC0001011. Some of the instrumentation used in this project was housed in the UNC SERC "Solar Energy Research Center Instrumentation Facility" funded by the U.S. Department of Energy−Office of Energy Efficiency & Renewable Energy under Award Number DE-EE0003188.

■ REFERENCES

(1) (a) Astruc, D.; Boisselier, E.; Ornelas, C. *Chem. Rev.* **2010**, *110*, 1857−1959. (b) Drain, C. M.; Varotto, A.; Radivojevic, I. *Chem. Rev.* **2009**, *109*, 1630−1658. (c) Szacilowski, K. *Chem. Rev.* **2008**, *108*, 3481−3548. (d) Hoeben, F. J. M.; Jonkheijm, P.; Meijer, E. W.; Schenning, A. *Chem. Rev.* **2005**, *105*, 1491−1546.

(2) (a) Lakowicz, J. R. *Principles of Fluorescence Spectroscopy*, 3rd ed.; Springer: New York, 2006. (b) McDonagh, C.; Burke, C. S.; MacCraith, B. D. *Chem. Rev.* **2008**, *108*, 400−422.

(3) (a) Meyer, T. J. *Acc. Chem. Res.* **1989**, *22*, 163−170. (b) Alstrum-Acevedo, J. H.; Brennaman, M. K.; Meyer, T. J. *Inorg. Chem.* **2005**, *44*, 6802−6827. (c) Gust, D.; Moore, T. A.; Moore, A. L. *Acc. Chem. Res.* **2009**, *42*, 1890−1898. (d) Gust, D.; Moore, T. A. *Science* **1989**, *244*, 35−41.

(4) (a) Du, P. W.; Schneider, J.; Luo, G. G.; Brennessel, W. W.; Eisenberg, R. *Inorg. Chem.* **2009**, *48*, 4952−4962. (b) Youngblood, W. J.; Lee, S. H. A.; Maeda, K.; Mallouk, T. E. *Acc. Chem. Res.* **2009**, *42*, 1966−1973. (c) Bonchio, M.; Carofiglio, T.; Carraro, M.; Fornasier, R.; Tonellato, U. *Org. Lett.* **2002**, *4*, 4635−4637.

(5) (a) Hsiao, J. S.; Krueger, B. P.; Wagner, R. W.; Johnson, T. E.; Delaney, J. K.; Mauzerall, D. C.; Fleming, G. R.; Lindsey, J. S.; Bocian, D. F.; Donohoe, R. J. *J. Am. Chem. Soc.* **1996**, *118*, 11181−11193. (b) Wagner, R. W.; Lindsey, J. S. *J. Am. Chem. Soc.* **1994**, *116*, 9759−9760. (c) Song, H.; Taniguchi, M.; Speckbacher, M.; Yu, L.; Bocian, D. F.; Lindsey, J. S.; Holten, D. *J. Phys. Chem. B* **2009**, *113*, 8011−8019. (d) Bellows, D.; Goudreault, T.; Aly, S. M.; Fortin, D.; Gros, C. P.; Barbe, J.-M.; Harvey, P. D. *Organometallics* **2010**, *29*, 317−325.

(6) (a) Jones, W. E.; Baxter, S. M.; Strouse, G. F.; Meyer, T. J. *J. Am. Chem. Soc.* **1993**, *115*, 7363−7373. (b) Dupray, L. M.; Meyer, T. J. *Inorg. Chem.* **1996**, *35*, 6299−6307. (c) Dupray, L. M.; Devenney, M.; Striplin, D. R.; Meyer, T. J. *J. Am. Chem. Soc.* **1997**, *119*, 10243−10244. (d) Friesen, D. A.; Kajita, T.; Danielson, E.; Meyer, T. J. *Inorg. Chem.* **1998**, *37*, 2756−2762. (e) Fleming, C. N.; Maxwell, K. A.; DeSimone, J. M.; Meyer, T. J.; Papanikolas, J. M. *J. Am. Chem. Soc.* **2001**, *123*, 10336−10347. (f) Sowash, G. G.; Webber, S. E. *Macromolecules* **1988**, *21*, 1608−1611. (g) Webber, S. E. *Chem. Rev.* **1990**, *90*, 1469−1482.

(7) (a) Marcaccio, M.; Paolucci, F.; Paradisi, C.; Roffia, S.; Fontanesi, C.; Yellowlees, L. J.; Serroni, S.; Campagna, S.; Denti, C.; Balzani, V. *J. Am. Chem. Soc.* **1999**, *121*, 10081−10091. (b) Campagna, S.; Denti, G.; Serroni, S.; Juris, A.; Venturi, M.; Ricevuto, V.; Balzani, V. *Chem.—Eur. J.* **1995**, *1*, 211−221. (c) Van Patten, P. G.; Shreve, A. P.; Lindsey, J. S.; Donohoe, R. J. *J. Phys. Chem. B* **1998**, *102*, 4209−4216. (d) Xu, Z. F.; Moore, J. S. *Acta Polym.* **1994**, *45*, 83−87. (e) Balzani, V.; Campagna, S.; Denti, G.; Juris, A.; Serroni, S.; Venturi, M. *Acc. Chem. Res.* **1998**, *31*, 26−34. (f) Tsukube, H.; Suzuki, Y.; Paul, D.; Kataoka, Y.; Shinoda, S. *Chem. Commun.* **2007**, 2533−2535. (g) Stapert, H. R.; Nishiyama, N.; Jiang, D. L.; Aida, T.; Kataoka, K. *Langmuir* **2000**, *16*, 8182−8188. (h) Ahn, T. S.; Thompson, A. L.; Bharathi, P.; Muller, A.; Bardeen, C. J. *J. Phys. Chem. B* **2006**, *110*, 19810−19819. (i) Nantalaksakul, A.; Reddy, D. R.; Bardeen, C. J.; Thayumanavan, S. *Photosynth. Res.* **2006**, *87*, 133−150. (j) Larsen, J.; Puntoriero, F.; Pascher, T.; McClenaghan, N.; Campagna, S.; Akesson, E.; Sundstrom, V. *ChemPhysChem* **2007**, *8*, 2643−2651. (k) Andersson, J.; Puntoriero, F.; Serroni, S.; Yartsev, A.; Pascher, T.; Polivka, T.; Campagna, S.; Sundstrom, V. *Faraday Discuss.* **2004**, *127*, 295−305. (l) Thomas, K. R. J.; Thompson, A. L.; Sivakumar, A. V.; Bardeen, C. J.; Thayumanavan, S. *J. Am. Chem. Soc.* **2005**, *127*, 373−383.

(8) (a) Giansante, C.; Raffy, G.; Schaefer, C.; Rahma, H.; Kao, M.-T.; Olive, A. G. L.; Del Guerzo, A. *J. Am. Chem. Soc.* **2011**, *133*, 316−325. (b) Babu, S. S.; Kartha, K. K.; Ajayaghosh, A. *J. Phys. Chem. Lett.* **2010**, *1*, 3413−3424. (c) Ajayaghosh, A.; Praveen, V. K.; Vijayakumar, C. *Chem. Soc. Rev.* **2008**, *37*, 109−122. (d) Bhattacharya, S.; Samanta, S. K. *Langmuir* **2009**, *25*, 8378−8381.

(9) Ferreira, K. N.; Iverson, T. M.; Maghlaoui, K.; Barber, J.; Iwata, S. *Science* **2004**, *303*, 1831−1838.

(10) (a) Hurley, D. J.; Tor, Y. *J. Am. Chem. Soc.* **1998**, *120*, 2194−2195. (b) Hurley, D. J.; Tor, Y. *J. Am. Chem. Soc.* **2002**, *124*, 3749−3762. (c) Hurley, D. J.; Tor, Y. *J. Am. Chem. Soc.* **2002**, *124*, 13231−13241. (d) Lewis, F. D.; Zhang, L. G.; Zuo, X. B. *J. Am. Chem. Soc.* **2005**, *127*, 10002−10003. (e) Holmlin, R. E.; Tong, R. T.; Barton, J. K. *J. Am. Chem. Soc.* **1998**, *120*, 9724−9725.

(11) Channon, K. J.; Devlin, G. L.; MacPhee, C. E. *J. Am. Chem. Soc.* **2009**, *131*, 12520−12521.

(12) Nam, Y. S.; Shin, T.; Park, H.; Magyar, A. P.; Choi, K.; Fantner, G.; Nelson, K. A.; Belcher, A. M. *J. Am. Chem. Soc.* **2010**, *132*, 1462−1463.

(13) (a) Stryer, L.; Haugland, R. P. *Proc. Natl. Acad. Sci.* **1967**, *58*, 719−726. (b) Pispisa, B.; Venanzi, M.; Palleschi, A.; Zanotti, G. *Macromolecules* **1994**, *27*, 7800−7808. (c) McGimpsey, W. G.; Chen, L.; Carraway, R.; Samaniego, W. N. *J. Phys. Chem. A* **1999**, *103*, 6082−6090. (d) Pispisa, B.; Stella, L.; Venanzi, M.; Palleschi, A.; Viappiani, C.; Polese, A.; Formaggio, F.; Toniolo, C. *Macromolecules* **2000**, *33*, 906−915. (e) Sahoo, H.; Roccatano, D.; Hennig, A.; Nau, W. M. *J. Am. Chem. Soc.* **2007**, *129*, 9762−9772.

(14) Photoexcited-state electron transfer is a phenomenon closely related to energy transfer and has been extensively studied in a number of different peptide systems. (a) Mecklenburg, S. L.; Peek, B. M.; Erickson, B. W.; Meyer, T. J. *J. Am. Chem. Soc.* **1991**, *113*, 8540−8542. (b) Mecklenburg, S. L.; Peek, B. M.; Schoonover, J. R.; McCafferty, D. G.; Wall, C. G.; Erickson, B. W.; Meyer, T. J. *J. Am. Chem. Soc.* **1993**, *115*, 5479−5495. (c) Mecklenburg, S. L.; McCafferty, D. G.; Schoonover, J. R.; Peek, B. M.; Erickson, B. W.; Meyer, T. J. *Inorg. Chem.* **1994**, *33*, 2974−2983. (d) McCafferty, D. G.; Bishop, B. M.; Wall, C. G.; Hughes, S. G.; Mecklenberg, S. L.; Meyer, T. J.; Erickson, B. W. *Tetrahedron* **1995**, *51*, 1093−1106.

(15) (a) Kozlov, G. V.; Ogawa, M. Y. *J. Am. Chem. Soc.* **1997**, *119*, 8377−8378. (b) Kornilova, A. Y.; Wishart, J. F.; Ogawa, M. Y. *Biochemistry* **2001**, *40*, 12186−12192. (c) Kornilova, A. Y.; Wishart, J. F.; Xiao, W. Z.; Lasey, R. C.; Fedorova, A.; Shin, Y. K.; Ogawa, M. Y. *J. Am. Chem. Soc.* **2000**, *122*, 7999−8006. (d) Fedorova, A.; Chaudhari, A.; Ogawa, M. Y. *J. Am. Chem. Soc.* **2003**, *125*, 357−362. (e) Fedorova, A.; Ogawa, M. Y. *Bioconjugate Chem.* **2002**, *13*, 150−154. (f) Hong, J.; Kharenko, O. A.; Ogawa, M. Y. *Inorg. Chem.* **2006**, *45*, 9974−9984.

(16) Crick, F. H. C. *Nature* **1952**, *170*, 882−883.

(17) (a) Talbot, J. A.; Hodges, R. S. *Acc. Chem. Res.* **1982**, *15*, 224−230. (b) Holtzer, A.; Holtzer, M. E. *Macromolecules* **1987**, *20*, 671−675.

(18) (a) Woolfson, D. N. *Adv. Protein Chem.* **2005**, *70*, 79−112. (b) Pandya, M. J.; Spooner, G. M.; Sunde, M.; Thorpe, J. R.; Rodger, A.; Woolfson, D. N. *Biochemistry* **2000**, *39*, 8728−8734. (c) Ryadnov, M. G.; Woolfson, D. N. *Angew. Chem., Int. Ed.* **2003**, *42*, 3021−3023. (d) Ryadnov, M. G.; Woolfson, D. N. *Nat. Mater.* **2003**, *2*, 329−332. (e) Ryadnov, M. G.; Woolfson, D. N. *J. Am. Chem. Soc.* **2004**, *126*, 7454−7455. (f) Mahmoud, Z. N.; Gunnoo, S. B.; Thomson, A. R.; Fletcher, J. M.; Woolfson, D. N. *Biomaterials.* **2011**, *32*, 3712−3720.

(19) (a) Oshea, E. K.; Klemm, J. D.; Kim, P. S.; Alber, T. *Science* **1991**, *254*, 539−544. (b) Harbury, P. B.; Zhang, T.; Kim, P. S.; Alber, T. *Science* **1993**, *262*, 1401−1407. (c) Woolfson, D. N.; Alber, T. *Protein Sci.* **1995**, *4*, 1596−1607.

(20) (a) Oshea, E. K.; Rutkowski, R.; Kim, P. S. *Cell* **1992**, *68*, 699−708. (b) Kohn, W. D.; Kay, C. M.; Hodges, R. S. *J. Mol. Biol.* **1998**, *283*, 993−1012. (c) Litowski, J. R.; Hodges, R. S. *J. Biol. Chem.* **2002**, *277*, 37272−37279. (d) Zhou, N. E.; Kay, C. M.; Hodges, R. S. *J. Mol. Biol.* **1994**, *237*, 500−512.

(21) (a) Lumb, K. J.; Kim, P. S. *Biochemistry* **1995**, *34*, 8642−8648. (b) Oakley, M. G.; Kim, P. S. *Biochemistry* **1998**, *37*, 12603−12610. (c) Gonzalez, L.; Woolfson, D. N.; Alber, T. *Nat. Struct. Biol.* **1996**, *3*, 1011−1018.

(22) (a) Lupas, A. *Trends Biochem. Sci.* **1996**, *21*, 375−382. (b) Marvin, D. A. *Curr. Opin. Struct. Biol.* **1998**, *8*, 150−158. (c) Herrmann, H.; Aebi, U. *Curr. Opin. Struct. Biol.* **1998**, *8*, 177−185. (d) Phillips, G. N.; Fillers, J. P.; Cohen, C. *J. Mol. Biol.* **1986**, *192*, 111−128. (e) McLachlan, A. D.; Karn, J. *J. Mol. Biol.* **1983**, *164*, 605−626.

(23) (a) Geisser, B.; Ponce, A.; Alsfasser, R. *Inorg. Chem.* **1999**, *38*, 2030−2037. (b) Kise, K. J.; Bowler, B. E. *Inorg. Chem.* **2002**, *41*, 379−386. (c) Kise, K. J.; Bowler, B. E. *Inorg. Chem.* **2003**, *42*, 3891−3897. (d) McCafferty, D. G.; Friesen, D. A.; Danielson, E.; Wall, C. G.; Saderholm, M. J.; Erickson, B. W.; Meyer, T. J. *Proc. Natl. Acad. Sci., U.S.A.* **1996**, *93*, 8200−8204.

(24) (a) Rostovtsev, V. V.; Green, L. G.; Fokin, V. V.; Sharpless, K. B. *Angew. Chem., Int. Ed.* **2002**, *41*, 2596−2599. (b) Tornoe, C. W.; Christensen, C.; Meldal, M. *J. Org. Chem.* **2002**, *67*, 3057−3064. (c) Meldal, M.; Tornoe, C. W. *Chem. Rev.* **2008**, *108*, 2952−3015.

(25) (a) Khan, S. I.; Beilstein, A. E.; Grinstaff, M. W. *Inorg. Chem.* **1999**, *38*, 418−418. (b) Khan, S. I.; Beilstein, A. E.; Smith, G. D.; Sykora, M.; Grinstaff, M. W. *Inorg. Chem.* **1999**, *38*, 2411−2415. (c) Khan, S. I.; Grinstaff, M. W. *J. Am. Chem. Soc.* **1999**, *121*, 4704−4705. (d) Khan, S. I.; Beilstein, A. E.; Tierney, M. T.; Sykora, M.; Grinstaff, M. W. *Inorg. Chem.* **1999**, *38*, 5999−6002. (e) Tierney, M. T.; Sykora, M.; Khan, S. I.; Grinstaff, M. W. *J. Phys. Chem. B* **2000**, *104*, 7574−7576.

(26) (a) Sonogashira, K.; Tohda, Y.; Hagihara, N. *Tetrahedron Lett.* **1975**, 4467−4470. (b) Chinchilla, R.; Najera, C. *Chem. Rev.* **2007**, *107*, 874−922. (c) Hobbs, F. W. *J. Org. Chem.* **1989**, *54*, 3420−3422.

(27) (a) Isaad, A. L. C.; Barbetti, F.; Rovero, P.; D'Ursi, A. M.; Chelli, M.; Chorev, M.; Papini, A. M. *Eur. J. Org. Chem.* **2008**, 5308−5314. (b) Cantel, S.; Isaad, A. L. C.; Scrima, M.; Levy, J. J.; DiMarchi, R. D.; Rovero, P.; Halperin, J. A.; D'Ursi, A. M.; Papini, A. M.; Chorev, M. *J. Org. Chem.* **2008**, *73*, 5663−5674.

(28) (a) Chan, T. R.; Hilgraf, R.; Sharpless, K. B.; Fokin, V. V. *Org. Lett.* **2004**, *6*, 2853−2855. (b) Lewis, W. G.; Magallon, F. G.; Fokin, V. V.; Finn, M. G. *J. Am. Chem. Soc.* **2004**, *126*, 9152−9153. (c) Juricek, M.; Stout, K.; Kouwer, P. H. J.; Rowan, A. E. *Org. Lett.* **2011**, *13*, 3494−3497.

(29) (a) Woody, R. W. *Biochem. Spectrosc.* **1995**, *246*, 34−71. (b) Greenfield, N. J. *Nat. Protoc.* **2006**, *1*, 2876−2890. (c) Hodges, R. S. *Biochem. Cell Biol.* **1996**, *74*, 133−154. (d) Zhou, N. E.; Zhu, B. Y.; Kay, C. M.; Hodges, R. S. *Biopolymers* **1992**, *32*, 419−426.

(30) (a) Zhou, N. E.; Kay, C. M.; Hodges, R. S. *Biochemistry* **1992**, *31*, 5739−5746. (b) Zhou, N. E.; Kay, C. M.; Hodges, R. S. *J. Biol. Chem.* **1992**, *267*, 2664−2670. (c) Su, J. Y.; Hodges, R. S.; Kay, C. M. *Biochemistry* **1994**, *33*, 15501−15510.

(31) (a) Pace, C. N. In *Methods in Enzymology*; Hirs, C. H. W., Timasheff, S. E. , Eds.; Academic Press: New York, 1986; Vol. *131*. (b) Defrancesco, R.; Pastore, A.; Vecchio, G.; Cortese, R. *Biochemistry* **1991**, *30*, 143−147.
(32) (a) Chen, Y. H.; Yang, J. T.; Chau, K. H. *Biochemistry* **1974**, *13*, 3350−3359. (b) Scholtz, J. M.; Qian, H.; York, E. J.; Stewart, J. M.; Baldwin, R. L. *Biopolymers* **1991**, *31*, 1463−1470. (c) Wendt, H.; Berger, C.; Baici, A.; Thomas, R. M.; Bosshard, H. R. *Biochemistry* **1995**, *34*, 4097−4107.
(33) (a) Kohn, W. D.; Kay, C. M.; Hodges, R. S. *Protein Sci.* **1995**, *4*, 237−250. (b) Serrano, L.; Horovitz, A.; Avron, B.; Bycroft, M.; Fersht, A. R. *Biochemistry* **1990**, *29*, 9343−9352.
(34) Juris, A.; Balzani, V.; Barigelletti, F.; Campagna, S.; Belser, P.; Vonzelewsky, A. *Coord. Chem. Rev.* **1988**, *84*, 85−277.
(35) (a) Dexter, D. L. *J. Chem. Phys.* **1953**, *21*, 836−850. (b) Förster, Th. *Discuss. Faraday Soc.* **1959**, *27*, 7−17. (c) Murtaza, Z.; Graff, D. K.; Zipp, A. P.; Worl, L. A.; Jones, W. E.; Bates, W. D.; Meyer, T. J. *J. Phys. Chem.* **1994**, *98*, 10504−10513.
(36) (a) Wang, G. Y.; Bergstrom, D. E. *Synlett* **1992**, 422−424. (b) Peek, B. M.; Ross, G. T.; Edwards, S. W.; Meyer, G. J.; Meyer, T. J.; Erickson, B. W. *Int. J. Pept. Protein Res.* **1991**, *38*, 114−123. (c) Telser, J.; Cruickshank, K. A.; Schanze, K. S.; Netzel, T. L. *J. Am. Chem. Soc.* **1989**, *111*, 7221−7226.
(37) Johnson, S. R.; Westmoreland, T. D.; Caspar, J. V.; Barqawi, K. R.; Meyer, T. J. *Inorg. Chem.* **1988**, *27*, 3195−3200.
(38) *The PyMOL Molecular Graphics System*, 1.2r3pre ed.; Schrödinger, LLC: New York.
(39) Frisch, M. J.; et al. *Gaussian 03*, Revision C.02; Gaussian, Inc.: Wallingford, CT, 2004.
(40) Case, D. A.; et al. *AMBER 11*; University of California: San Francisco, CA, 2010.
(41) Hornak, V.; Abel, R.; Okur, A.; Strockbine, B.; Roitberg, A.; Simmerling, C. *Proteins: Struct., Funct., Bioinf.* **2006**, *65*, 712−725.
(42) Lee, C. T.; Yang, W. T.; Parr, R. G. *Phys. Rev. B* **1988**, *37*, 785−789.
(43) (a) Hay, P. J.; Wadt, W. R. *J. Chem. Phys.* **1985**, *82*, 270−283. (b) Hay, P. J.; Wadt, W. R. *J. Chem. Phys.* **1985**, *82*, 299−310. (c) Wadt, W. R.; Hay, P. J. *J. Chem. Phys.* **1985**, *82*, 284−298.
(44) Bayly, C. I.; Cieplak, P.; Cornell, W. D.; Kollman, P. A. *J. Phys. Chem.* **1993**, *97*, 10269−10280.
(45) Brandt, P.; Norrby, T.; Akermark, E.; Norrby, P. O. *Inorg. Chem.* **1998**, *37*, 4120−4127.